A novel method for diagnosing land-atmosphere coupling sensitivity in a single-column model

Finley M. Hay-Chapman,[1] Paul A. Dirmeyer,[1,2].

[1] *George Mason University, Fairfax, Virginia*

[2] *Center for Ocean-Land-Atmosphere Studies, Fairfax, Virginia*

Corresponding author: Finley M. Hay-Chapman, fhaychap@gmu.edu

Early Online Release: This preliminary version has been accepted for publication in *Journal of Hydrometeorology*, may be fully cited, and has been assigned DOI 10.1175/JHM-D-22-0237.1. The final typeset copyedited article will replace the EOR at the above DOI when it is published.

ABSTRACT

The response of boundary layer properties and cloudiness to changes in surface evaporative fraction (EF) is investigated in a single-column model to quantify the locally coupled impact of sub-grid surface variations on the atmosphere during summer. Sensitive coupling days are defined when the model atmosphere exhibits large variations across a range of EF centered on the analyzed value. Coupling sensitivity exists as both positive (cloudiness increases with EF) and negative (clouds increase with decreasing EF) feedback regimes. The positive regime manifests in shallow convection situations, which are capped by a strengthened inversion and subsidence, restricting the vertical extent of convection to just above the boundary layer. Surfaces with larger EF (greater surface latent heat flux) can inject more moisture into the vertically confined system, lowering the cloud base and an increasing cloud liquid water path (LWP). Negative feedback regimes tend to manifest when large-scale deep convection, such as from mesoscale convective systems and fronts, is advected through the domain, where convection strengthens over surfaces with a lower EF (greater surface sensible heat flux). The invigoration of these systems by the land surface leads to an increase in LWP through strengthened updrafts and stronger coupling between the boundary layer and the free atmosphere. These results apply in the absence of heterogeneity-induced mesoscale circulations, providing a one-dimensional dynamical perspective on the effect of surface heterogeneity. This study provides a framework intermediate complexity, lying between parcel theory and high-resolution coupled land-atmosphere modeling, and therefore isolates the relevant first-order processes in land-atmosphere interactions.

SIGNIFICANCE STATEMENT

Cloud formation, distribution, and other properties may be sensitive to heterogeneous surfaces depending on the strength and location of such heterogeneities and the background atmospheric state. This may drive differences in the cloud population depending on which part of the domain one is located. This may also lead to mesoscale circulations, which may strengthen or weaken this effect. Currently, climate models act on scales (~100 km) that are too large to explicitly represent these processes, which are strongest at smaller scales (around 5-40 km). Therefore, sub-grid scale heterogeneity is neglected, and any predictability and model fidelity it may provide is lost. We use a simple model to diagnose sensitivity of the local atmosphere to surface variations meant to represent possible sub-grid heterogeneity, providing a first-order estimate of its effect. We conclude that preferentially sensitive atmospheric states exist that lead to positive and/or negative feedback between land and atmosphere. This information is valuable to future climate model parameterizations aimed at improving the representation of these feedbacks.

Accepted for publication in *Journal of Hydrometeorology*. DOI 10.1175/JHM-D-22-0237.1.

1. Introduction

Land-atmosphere (L-A) interactions are known to play a major role in determining continental weather and climate (Santanello et al., 2018). Evaluating the strength and behavior of this coupling has been an ongoing topic of research since the land surface was first identified as a source of predictability in the climate system (Shukla & Mintz, 1982). The role of the land surface has been explicitly accounted for in coupled climate models by using land surface models (LSMs) as a dynamic lower boundary condition to the atmosphere. However, a persistent challenge is the disconnection between the spatial scales at which the land surface influences local processes such as boundary layer growth (turbulent- to meso-scales) and the coarser resolution (meso- to synoptic-scales) at which weather and climate models are typically run (Kawashima & Ishida, 1992; Entekhabi, 1995; Roy & Avissar, 2000). Because of this, processes that dictate the influence of the sub-grid (0.1-10 km for today's models) land surface heterogeneities on grid-scale atmospheric conditions need to be parameterized (Manabe et al., 1965; Henderson-Sellers et al., 1993; Letzel & Raasch, 2003; Huang & Margulis, 2012).

Many current LSMs incorporate land surface heterogeneity by using a sub-grid mosaic of tiles representing fractions of different land cover/land use types within each grid cell (Avissar & Pielke, 1989; Koster & Suarez, 1992; Lawrence et al., 2019). This allows an LSM to compute separate responses to the atmospheric state; how much each tile contributes to the grid cell mean value is based on its fractional coverage without regard to spatial structure. Individual tile contributions are aggregated when the area weighted average of states and fluxes is passed to the atmospheric model. This is a hindrance, as spatial averaging removes any signal of the dynamically induced response that may be produced by heterogeneity, leading to model errors and biases.

Sub-grid scale heterogeneity that can induce a dynamic atmospheric response may be driven by variations in land use/land cover type (e.g. vegetated vs. bare soil), soil type (e.g. clay vs. sandy soils), topography, local geology (e.g karst vs. non-karst geomorphology), and/or spatial variations in soil moisture (SM) left after scattered precipitation events (i.e. meteorologically forced heterogeneity) (Tian et al., 2022; Chen et al., 2020; Norton, 2018; Dirmeyer & Norton, 2018; Simon et al., 2021). Depending on their spatial structure and the large-scale atmospheric state, such characteristics of the land surface may produce a response in the development of the daytime planetary boundary layer (PBL), local convection, cloud formation/structure, and precipitation (Avissar & Schmidt, 1998; Taylor

Accepted for publication in *Journal of Hydrometeorology*. DOI 10.1175/JHM-D-22-0237.1.

& Ellis, 2006; Huang & Margulis, 2009; van Heerwaarden et al., 2009; van Heerwaarden et al., 2010; Huang & Margulis, 2012; van Heerwaarden et al., 2014; Kang & Ryu, 2016; Lee et al., 2019; Omidvar et al., 2020; Harvey et al., 2022). This has been shown in both observations and fine-resolution LESs. These processes may drive secondary, mesoscale circulations that may act to strengthen or weaken the atmospheric response, although the effects of such circulations are beyond the scope of this work. Nevertheless, the role of the dynamic influence of land surface heterogeneity has become a major topic of research and climate model development, and many argue for improvements upon the mosaic tile approach in LSMs and how the land surface interacts with the atmospheric model (Liu et al., 1999; Taylor et al., 2013; Machulskaya & Mironov, 2018; Huang et al., 2022).

A commonly used quantity in L-A coupling studies is the surface evaporative fraction (EF), defined as the ratio of latent heat flux to the net available energy at the land surface (i.e., the sum of the latent heat (LH) and sensible heat (SH) fluxes):

$$EF = \frac{LH}{LH + SH} \tag{1}$$

EF is a good choice to quantify the varied flux partitioning states induced by land surface heterogeneity, and therefore drive an atmospheric response, due to its ability to capture the combined effect of both SH and LH. Additionally, EF is the link between the land surface states and the PBL (through the partitioning of surface fluxes of heat and moisture fluxes that alter air temperature and humidity), and it has many applications over a large range of spatial and temporal scales (Dirmeyer et al., 2000; Bezerra et al., 2013; Ford et al., 2014; Williams & Torn, 2015; Ukkola et al., 2018; Zhang et al., 2019; Yang et al., 2021).

Both surface heat fluxes play key roles in L-A coupling and PBL processes. SH drives heating and upward mixing of the PBL through driving turbulence and updrafts, potentially affecting cloud formation (Shin & Ha, 2007; Bosman et al., 2018; Kim & Kwon, 2019), and can be a key factor in the intensification and prolongation of heat waves and drought (Roundy & Wood, 2015; Ford et al., 2018; Benson et al., 2021; Dirmeyer et al., 2021); LH moistens the PBL, acting to lower the cloud base and alter cloud cover and distribution (Ek & Holtslag, 2004; Betts, 2009; Qian et al., 2013; Zheng et al., 2021; Wei et al., 2021; Hsu et al., 2022). Depending on the atmospheric profile, the land surface, and other factors such as incoming solar radiation, the feedbacks between land and atmosphere may be more sensitive to one flux component than the other (Findell & Eltahir, 2003a; Findell & Eltahir, 2003b; Koster et al., 2006; Guo et al., 2006; Guillod et al., 2015; Tawfik

Accepted for publication in *Journal of Hydrometeorology*. DOI 10.1175/JHM-D-22-0237.1.

et al., 2015a&b; Santanello et al., 2018; Hsu et al., 2021), and will likely intensify or shift location under climate change (Seneviratne et al., 2010; Dirmeyer et al., 2012; Dirmeyer et al., 2013).

Differences in sensitivity to certain components in the local L-A coupling processes have been referred to as wet/dry advantage (Findell et al., 2003a; Findell & Eltahir, 2003b), moisture/energy-limited (Budyko, 1974; Sposito, 2017), or positive/negative feedback regimes (Brunsell, 2006; Qiu & Williams, 2020). These coupling regimes may be defined by a variety of factors, but in general they tend to be location and time dependent (Koster et al., 2006; Guo & Dirmeyer, 2013; Roundy et al., 2013; Catalano et al., 2016). Additionally, feedbacks may have differing effects depending on whether they are evaluated spatially or temporally, and on the scales (both spatial and temporal) considered. For example, Findell et al. (2011) conducted a study, using the North American Regional Reanalysis (resolution ~80km), on the sensitivity of convective triggering and accumulated precipitation to the EF over time. This study determined the climatology of coupling between these variables rather than the local processes involved in the feedback. They found that for much of the United States and Mexico, EF had a strong positive feedback on convective triggering in the PBL (i.e. a higher EF (wetter surface) over a given time led to a higher frequency of convective triggering).

An observational study conducted by Taylor et al. (2011) found a seemingly contradictory result: the existence of a strong negative feedback between the surface states and convective initiation. That study focused on the *spatial* structure of land surface properties and their role in the feedbacks. Their conclusion, over a domain within the Sahel, was that convection was more often triggered over dry surfaces. Additionally, they concluded that this effect was enhanced over areas with large soil moisture gradients, indicating a large degree of surface heterogeneity. This effect was strongest on spatial scales of heterogeneity on the order of 10-40 km. A subsequent study by Klein & Taylor (2020) found that mesoscale convective systems were enhanced when they passed over surfaces with stronger SH in regions having sharp gradients in EF.

Guillod et al. (2015) reconciled these conflicting results for surface-convective feedbacks, using remote sensing data. They showed that both feedbacks may exist; one based on temporal variations and the other spatial patterns, and that convection is most likely to be triggered over regions that are anomalously wet in time but have strongly

Accepted for publication in *Journal of Hydrometeorology*. DOI 10.1175/JHM-D-22-0237.1.

heterogeneous surface states. When convection was triggered, it tended to occur over the drier part of the domain.

Conflicting L-A feedbacks have been reported in modeling studies as well. Studies involving models with coarse spatial resolutions have reported stronger positive feedbacks between SM/EF and convection/clouds (Hohenegger et al., 2009; Taylor et al., 2013; Moon et al., 2019), while high-resolution convection-permitting models and large-eddy simulations (LES) tend to report negative feedbacks (Kang & Bryan, 2011; Chen et al., 2020; Simon et al., 2021; Gaal & Kinter, 2021). GCMs are usually not able to resolve the scales needed to capture important features of surface heterogeneity, so when a given grid cell has more moisture at the surface, there is usually an increased cloud response. Meanwhile, LESs resolve the spatial scales needed to trigger a heterogeneous land-atmosphere coupling response and tend to exhibit feedback behavior more consistent with observations.

There are many processes affecting land-atmosphere coupling, especially in the presence of surface heterogeneity. We choose to focus on the sensitivity of the PBL to the effects of surface variations, quantified as a range of EF given identical available energy. This encompasses the possible effects of heterogeneity in soil moisture, land cover and soil types together, but excluding topographic forcing. We attempt to answer the question: Under what conditions does the atmosphere exhibit a heightened sensitivity to surface variations, and therefore surface heterogeneity? The simplicity of a single-column model is exploited to survey a range of surface conditions with the same large-scale atmospheric forcing to isolate the effect of the surface variability. Heterogeneity-induced circulations are not explicitly considered in this framework, only the varying response of the local atmospheric column.

In subsequent sections we introduce a method to determine atmospheric sensitivity to surface flux partitioning perturbations and demonstrate its ability to answer the research question outlined above.. The methodology is described in Section 2. Results are presented in Section 3. In Section 4, we discuss how this method relates to prior research and how it may be used in future studies.

2. Methodology

In this study, we carry out a set of model experiments with version 6 of the Single Column Atmosphere Model (SCAM6; Gettelman et al. 2019), to quantify atmospheric states having increased coupling sensitivity to sub-grid surface conditions that may arise due to land surface heterogeneity. SCAM6 is available as a part of the Community Atmosphere Model

Accepted for publication in *Journal of Hydrometeorology*. DOI 10.1175/JHM-D-22-0237.1.

(CAM) version 6 within the Community Earth System Model (CESM) version 2.1.1 (Danabasoglu et al., 2020). Single-column models (SCMs) are fundamentally single grid cell columns of global circulation models (GCMs), and prognose atmospheric variables for a single location in the presence of a prescribed, evolving large-scale atmospheric state. The relevant grid scale for SCAM6 is the T42 grid provided within CESM2, corresponding to ~250 km spatial resolution. We employ a novel approach that allows us to examine coupling sensitivity to the conditions of a spatially varying surface. This method uses an ensemble of simulations where each ensemble member is subject to a different, time-evolving surface constrained by prescribed values of EF, while initial states and large-scale atmospheric forcing are identical. The varying surface EF within an ensemble are meant to represent the range of potential surface conditions present within a heterogeneous domain the size of a GCM grid cell. By comparing members of this ensemble to each other and a control simulation forced with the observed surface state, we may quantify a potential coupling sensitivity to varying surface conditions.

a. Model Configuration

Because SCAM6 only predicts the evolution of a single atmospheric column, boundary conditions (BCs) must be specified via a large-scale forcing dataset. We generate BCs from the constrained variational analysis (VARANAL) product (Xie et al., 2004; Tang et al., 2019) for the atmospheric radiation measurement (ARM) Southern Great Plains (SGP) site in Northern Oklahoma (36.61° N, 97.49° W), provided through the ARM Data Discovery online archive (https://adc.arm.gov/discovery/). The most recent version of VARANAL provides observationally-based hourly forcing data at 25 hPa vertical intervals over the SGP site from May 1, 2012 to August 31, 2019, representative of a circular horizontal footprint of diameter ~300 km. For the lateral BCs, VARANAL provides SCAM with large-scale flow (U, V), as well as its associated advective tendencies for temperature (T) and water vapor mixing ratio (Q). The lower boundary is controlled by prescribed turbulent fluxes of sensible (SH) and latent (LH) heat, and the surface skin temperature. The sum SH+LH represents a prescribed available energy.

To keep the model close to the observed large-scale state, especially in the upper atmosphere, temperature is relaxed to the large-scale values given by VARANAL. A relaxation e-folding timescale of 2 days is applied at the top of the atmospheric column and 10 days at the surface, with a linear ramping in between the two. This allows SCAM6 physics to dominate the tendencies within the boundary layer, where processes act on

Accepted for publication in *Journal of Hydrometeorology*. DOI 10.1175/JHM-D-22-0237.1.

timescales much shorter than 10 days (Dal Gesso & Neggers, 2017). Shorter relaxation timescales above the PBL allow for a more accurate large-scale state in the free troposphere - even in the presence of errors in the dynamical forcing (Gettelman et al., 2019). With this relaxation, the prognostic equation for temperature gains an extra term:

$$\frac{\partial T}{\partial t} = \cdots + \frac{1}{\tau(z)}\left(T(t) - T_{obs}(t)\right) \tag{2}$$

where $\tau(z)$ is the level-dependent relaxation timescale.

We restrict our analyses to the years 2012 to 2018 during the warm season from June through September (JJAS), when land-atmosphere coupling and convective activity is strongest. For each year's JJAS period, there is both a control run (CTRL) and an ensemble of 19 altered surface runs (ALT). For all runs, we follow a 2-day hindcast approach (Ma et al. 2015) where a simulation is initiated every day at 0000 LST and is run for 2 days. The second day of each simulation is concatenated into a continuous dataset for each year spanning from the beginning of June 1st until the end of September 29th. This approach avoids long-term biases and drift found in long continuous simulations, allowing for a cleaner comparison between separate surface forcings for any given day and a free atmosphere that is well-constrained by the large-scale forcing (Ma et al. 2015, Huang et al. 2022). For any day the large-scale atmospheric forcings for the CTRL run and each of its respective ALT runs are identical; the only difference is in the surface flux partitioning. For a given ALT run, we constrain the surface state to adhere to a constant evaporative fraction (EF) for time steps when EF from VARANAL is positive. This predominantly impacts the surface fluxes between sunrise and sunset, when both sensible and latent heat fluxes are positive. Consequentially, surface forcing is equivalent across runs when EF is negative; this usually occurs during nighttime hours. More specifically, we define the altered surface forcing as such: each ALT run corresponds to a given EF across the spectrum spanning 0.05 to 0.95 in increments of 0.05. This way, only the surface flux partitioning is changed, not the amount of available energy at the surface. This approach allows us to examine how the grid-scale atmosphere responds across a range of prescribed EFs, as the large-scale atmospheric forcing remains identical.

b. Coupling Sensitivity Score

To quantify atmospheric sensitivity to varying EF, we define a metric called the coupling sensitivity score (CSS). CSS measures the perturbations of a given target variable,

Accepted for publication in *Journal of Hydrometeorology*. DOI 10.1175/JHM-D-22-0237.1.

X, when subjected to variations in surface EF. For each day, there are two terms: CSS_+ and CSS_-, which measure the strength of positive and negative feedbacks, respectively. To compute the CSS, we first take a subset of ALT ensemble members whose surface states are nearest to the CTRL run's value of EF ($EF_{ALT_i} \approx EF_{CTRL}$). We first identify the ensemble member whose EF is closest to the daytime average (0900-1700 LST) EF in the CTRL run. We call this member ALT_C (C standing for "closest"). The daytime average EF is computed by inserting the daytime mean of SH and LH into Eq. (1). The subset is then defined as the 7 ALT runs whose surface EF span the range ±0.15 of EF_{ALT_C}. This range, which we call the "sensitivity window", is chosen to detect variations in coupling behavior in the immediate vicinity of the mean surface state, replicating most of the sub-grid states likely to be found in the domain. It is likely for the range of EF within such a domain to be larger, however: e.g., paved surfaces and open water bodies will tend toward opposite extremes of EF. We have chosen this conservative window to focus on sub-grid states that are *most* likely to be present (i.e. those closest to the mean state) due to variations in soil moisture, soil properties and land cover.

Each ensemble member within the sensitivity window is meant to represent a local surface flux partitioning state that may exist within the domain the size of a GCM grid cell. We note that there are 12 out of 840 simulation days where $EF_{ALT_C} \geq 0.85$. When this occurs, there are fewer than three ALT ensembles members with $EF_{ALT_i} \geq EF_{ALT_C}$, and so the CSS is computed over the range: $0.65 \leq EF \leq 0.95$. This has minimal effect on the results, however, as none of these 12 days had large L-A coupling sensitivity as indicated by the CSS.

We compute the gradient using second order accurate central difference approximations of target variable *X* with respect to *EF* for all ALT ensemble members (for the edge values EF = [0.05, 0.95], first order forward/backward differences are used). Finally, CSS_+ and CSS_- are defined as the maximum and minimum values of $\partial X/\partial(EF)$, respectively, from only those ensemble members within the sensitivity window.

$$CSS_+ = max\left\{\frac{\partial X}{\partial(EF)}\right\}_{window} \quad (>0)$$

$$CSS_- = min\left\{\frac{\partial X}{\partial(EF)}\right\}_{window} \quad (<0) \qquad (3)$$

Accepted for publication in *Journal of Hydrometeorology*. DOI 10.1175/JHM-D-22-0237.1.

If $CSS_+ < 0$ or $CSS_- > 0$, they are reset to zero, indicating no feedback of that sign was detected.

Finally, we define a "sensitive coupling day" as any day that has a CSS_+ and/or CSS_- whose *magnitude* is in the 5th percentile tails of their distributions across all days for all years in the analysis, excluding clear sky days, to isolate the effect of the surface on moist convection. We define clear sky days as any day in which afternoon average (1200-1700 LST) cloud liquid water path (LWP) falls under a threshold of 0.005 kg/m^2 for *all ensemble members within the sensitivity window*. With this definition, 206 clear sky days were identified out of 840 total days. A sensitive coupling day specified by large CSS_+ is referred to as a positive feedback day, whereas one specified by a large CSS_- is referred to as a negative feedback day. It is possible for one day to register as both a positive and negative feedback day if large magnitudes of CSS_+ and CSS_- coexist within that day's sensitivity window. With this definition, there are 32 sensitive coupling days specified for each feedback regime out of a total of 634 non-clear days, with only 3 of the 634 days identified as having both regimes (2 of the days with both regimes have a maximum value of $\partial X/\partial(EF)$ within the sensitivity window, with decreasing values towards both the wetter and drier ends of the EF spectrum; the other day has the opposite, where a minimum value of $\partial X/\partial(EF)$ is located within the sensitivity with increasing values in either direction (not shown)).

For this study, we use the afternoon average LWP as the target variable, X; henceforth, any variable denoted as an "afternoon average" indicates an average over 1200-1700 LST. LWP is chosen for its ability to represent changes in cloud characteristics within the column as a scalar, and under hydrostatic conditions is defined as: $LWP = \int_0^{p=p_0} r_- \frac{dp}{g}$, where r_L is the liquid water mixing ratio, g is the gravitational constant, and p_0 is a reference pressure; p_0=1,000 hPa in SCAM6, at the surface of its hybrid pressure-sigma vertical grid. LWP is especially sensitive to changes in low- and mid-level convective clouds (due to their higher moisture content), while being relatively insensitive to high clouds (Huang et al., 2015). Using LWP also allows for correspondence between CSS-identified positive and negative feedback regimes and the canonical energy-limited (i.e., dry advantage) and moisture-limited (i.e., wet advantage) L-A coupling regimes. Because of the methodology, $\partial(EF)$ in Eq. (3) is always 0.1, so with LWP as the target variable the equation of CSS may be simplified to:

Accepted for publication in *Journal of Hydrometeorology*. DOI 10.1175/JHM-D-22-0237.1.

$$CSS_{+} = max\left\{\frac{\partial(LWP)}{0.1}\right\}_{window} \quad (>0)$$
$$CSS_{-} = min\left\{\frac{\partial(LWP)}{0.1}\right\}_{window} \quad (<0) \qquad (4)$$

Fig. 1a provides a visual aid for understanding the CSS. It shows the timeseries of $\partial(LWP)/\partial(EF)$ for all ALT ensemble members (along the y-axis) in the 2014 season (along the x-axis). For CSS computation, only the gradient values that fall within the sensitivity window (dotted black lines) each day are considered. Overall, larger magnitudes of CSS_{+} or CSS_{-} are sporadic for this year, with many days effectively insensitive to surface variations – i.e., there are a few days with large gradients (dark colors) observed to be within the sensitivity window; on most days, gradients are weak (pale colors). On the bottom row, the left and middle panels provide examples for a positive feedback day and a negative feedback day, respectively. One of the three days in this study where both feedbacks occur is shown in the right panel. For the positive feedback day (Fig. 1b), EF_{ALT_C} = 0.5, and cloud cover and LWP are more enhanced over the wet surfaces (higher EFs) than the dry ones (lower EFs). Within the sensitivity window, LWP has a minimum of 0.0 kg m^2 for EF < 0.5 and a maximum of ~0.2 kg m^2 at EF = 0.65; the maximum cloud cover fraction for any ensemble member within the sensitivity window has a minimum of ~0.1 and a maximum of ~1.0. For the negative feedback day (Fig. 1c), EF_{ALT_C} = 0.7, and the opposite occurs, a dry advantage. On this day, LWP has a minimum of 0.0 kg m^2 at EF = 0.85 and a maximum of ~0.15 kg m^2 at EF = 0.7. The maximum cloud cover fraction for any ensemble member within the sensitivity window has a minimum of 0.0 and a maximum of ~0.3. For the day where both feedbacks exist (Fig. 1d), there is a narrow range of EFs within the window (around 0.5) with increased LWP, however, increasing or decreasing the EF from these values results in a noteworthy decrease in cloud content.

Accepted for publication in *Journal of Hydrometeorology*. DOI 10.1175/JHM-D-22-0237.1.

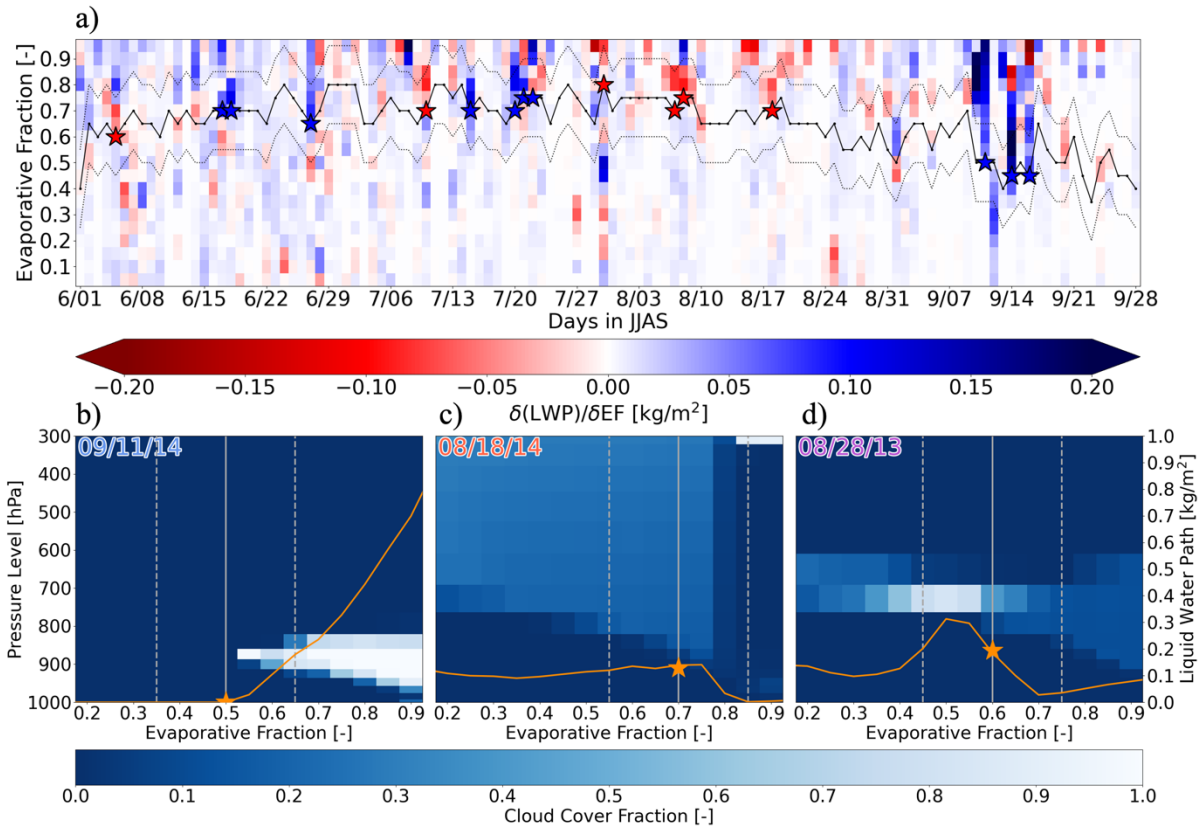

Fig. 1. Top: a) afternoon average $\partial(LWP)/\partial(EF)$ in shading for each day (x-axis) and surface EF (y-axis) for the 2014 season, solid black line indicates EF_{ALT_C} with a ±0.15 sensitivity window in dotted black, days identified as sensitive are starred with positive feedback in blue and negative feedback in red. Bottom: For 3 specific days, cloud cover fraction in shading for each pressure level (left y-axis) and ALT ensemble EF (x-axis) overlaid by vertically integrated LWP (right y-axis) from ALT runs (orange lines) and the CTRL run (orange star); vertical lines for EF_{ALT_C} are in solid grey surrounded by ±0.15 sensitivity window in dashed grey for one positive feedback day in (b), a negative feedback day in (c) and a both feedbacks day (from 2013) in (d).

c. Significance Testing

Statistical significance in this study is determined by computing confidence intervals with the bias-corrected accelerated bootstrap technique (Efron, 1987; Efron & Tibshirani, 1993). This method is provided in the stats module of the SciPy Python library, which we use in our analysis. Non-parametric methods, like the bootstrap, make no assumptions about the data distribution, and the bias-corrected accelerated technique is well-suited for sets of unequal sample sizes.

3. Results

a. Method Validation

Accepted for publication in *Journal of Hydrometeorology*. DOI 10.1175/JHM-D-22-0237.1.

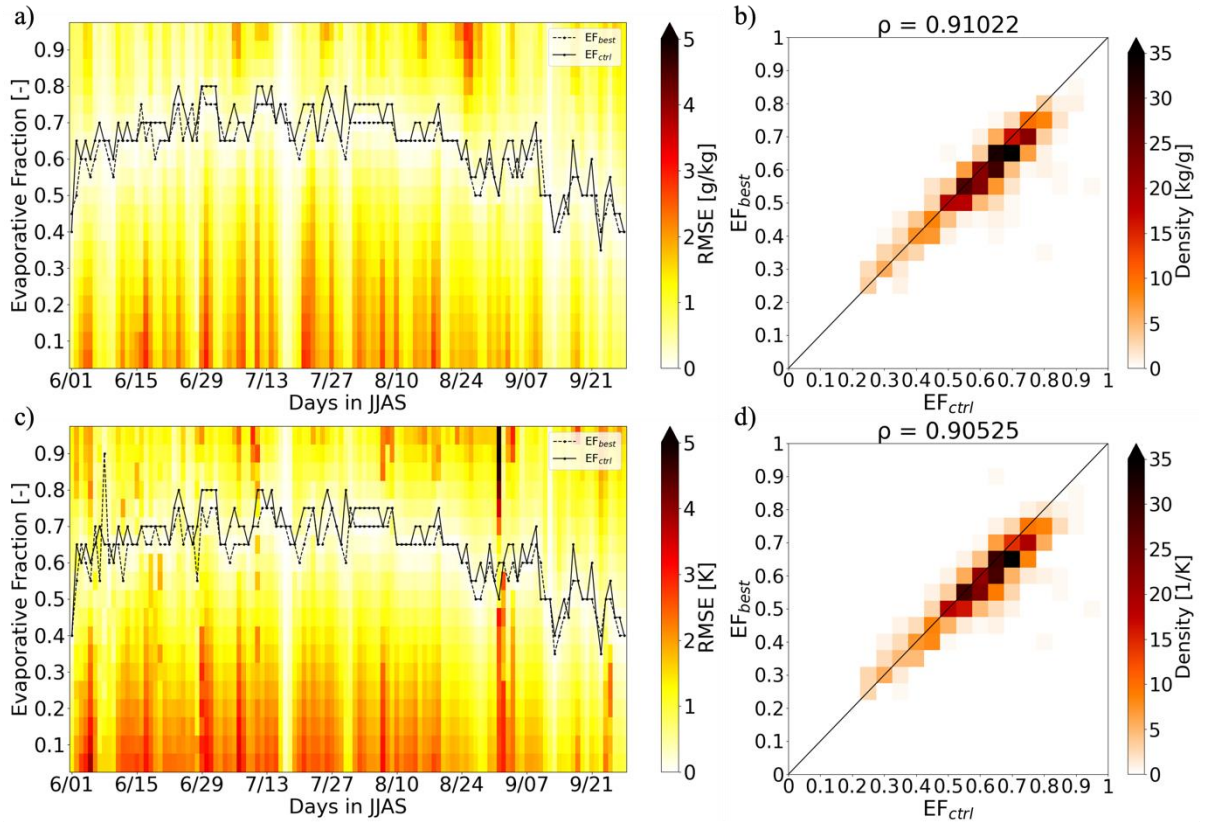

Fig. 2. RMSE for profiles in shading for Q (a) and T (c) over the 2014 period for each ALT SCAM run, overlaid by the time series of EF from VARANAL data (solid line) and the ALT SCAM with minimum RMSE compared to the CTRL SCAM run (dotted line); Bivariate probability density functions of EF_{ctrl} and EF_{best} for the *entire* analysis period in shading for Q (b) and T (d), black lines represent EF_{ctrl}=EF_{best}.

Fig. 2a and 2c show the root mean square error (RMSE) for the atmospheric profiles (surface up to 200 hPa) of afternoon average Q and T, respectively, between the control run and each of member of ALT for the 2014 season (in shading). To compute the mean RMSE for each day, vertical levels are pressure-weighted according to each level's thickness. Overlaid on those same plots are the time series of the daytime average EF from VARANAL (solid line), which we take here as the "truth", and the time series of EF corresponding to the ensemble member that has the minimum error for a given day (dotted line). We refer to these values as EF_{ctrl} and EF_{best}, respectively; their time series are highly correlated, showing that model profiles with time-varying EF are adequately reproduced when prescribing a constant surface EF throughout the day. Fig. 2b and 2d show bivariate probability density functions (PDFs) of EF_{ctrl} and EF_{best} covering all years in the study period, for T and Q, respectively. Each measure has a correlation of 0.91. Both also have a

File generated with AMS Word template 2.0

Accepted for publication in *Journal of Hydrometeorology*. DOI 10.1175/JHM-D-22-0237.1.

small but statistically significant (95% confidence) negative mean bias error (MBE) in EF: MBE_T = -0.0283, MBE_Q = -0.0273. This bias is acceptable for this study, given that the minimum EF increment for the ensemble is almost double the magnitude of MBE. The high correlation and low error give confidence that the ensemble members corresponding to EF_{best}, for a given day, reliably represent the CTRL run. Furthermore, mean RMSE for temperature and moisture profiles over the entire analysis period when comparing CTRL with VARANAL are 1.84 K and 0.842 g kg^{-1}, respectively (not shown). These errors are acceptable for this study, as there are much larger differences between ALT ensemble members than there are between CTRL and VARANAL.

b. Sensitive Days

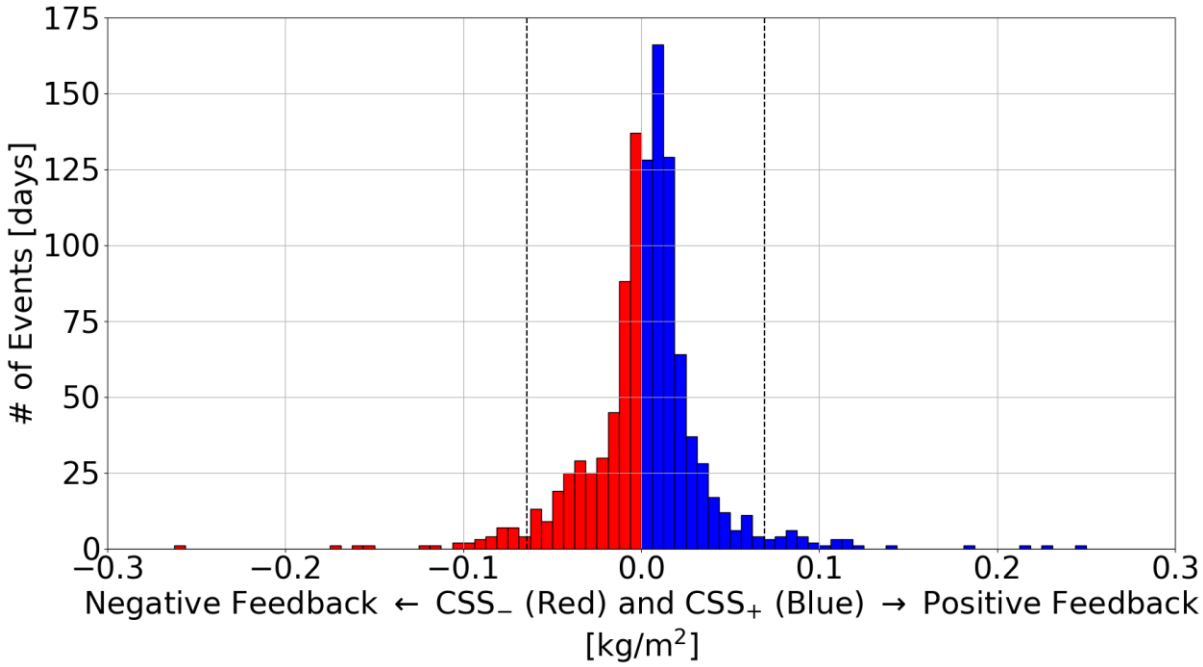

Fig. 3. Frequency distributions of CSS_- (red) and CSS_+ (blue); y-axis shows the number of events, in days, for each bin on the x-axis. Dotted black lines represent sensitivity thresholds (5^{th} percentile for CSS_-, 95^{th} percentile for CSS_+).

Fig. 3 shows the distributions of CSS_+ and CSS_- values, with sensitive thresholds marked for each by a dashed black line (5^{th} percentile for CSS_-, 95^{th} percentile for CSS_+). While each distribution has a similar, long tail of extreme events, the distributions are not symmetrical. This shows that positive and negative feedbacks do not behave the same way or occur at the same frequency, depending on magnitude. The most common outcome in the positive regime is a small positive feedback ($0.02 \leq CSS_+ \leq 0.04$), while fewer events with

Accepted for publication in *Journal of Hydrometeorology*. DOI 10.1175/JHM-D-22-0237.1.

no feedback are detected ($CSS_+ \leq 0.01$). Contrarily, the most common event in the dry advantage regime is that no feedback was detected ($CSS_- \geq -0.01$). Additionally, strong coupling sensitivity ($|CSS| > 0.1$) occurs more frequently in the wet advantage regime, with 13 days indicating strong positive feedback compared to 8 days indicating a strong negative feedback.

1) PBL EVOLUTION & MIXING DIAGRAMS

(i) Flux Partitioning & PBL Growth

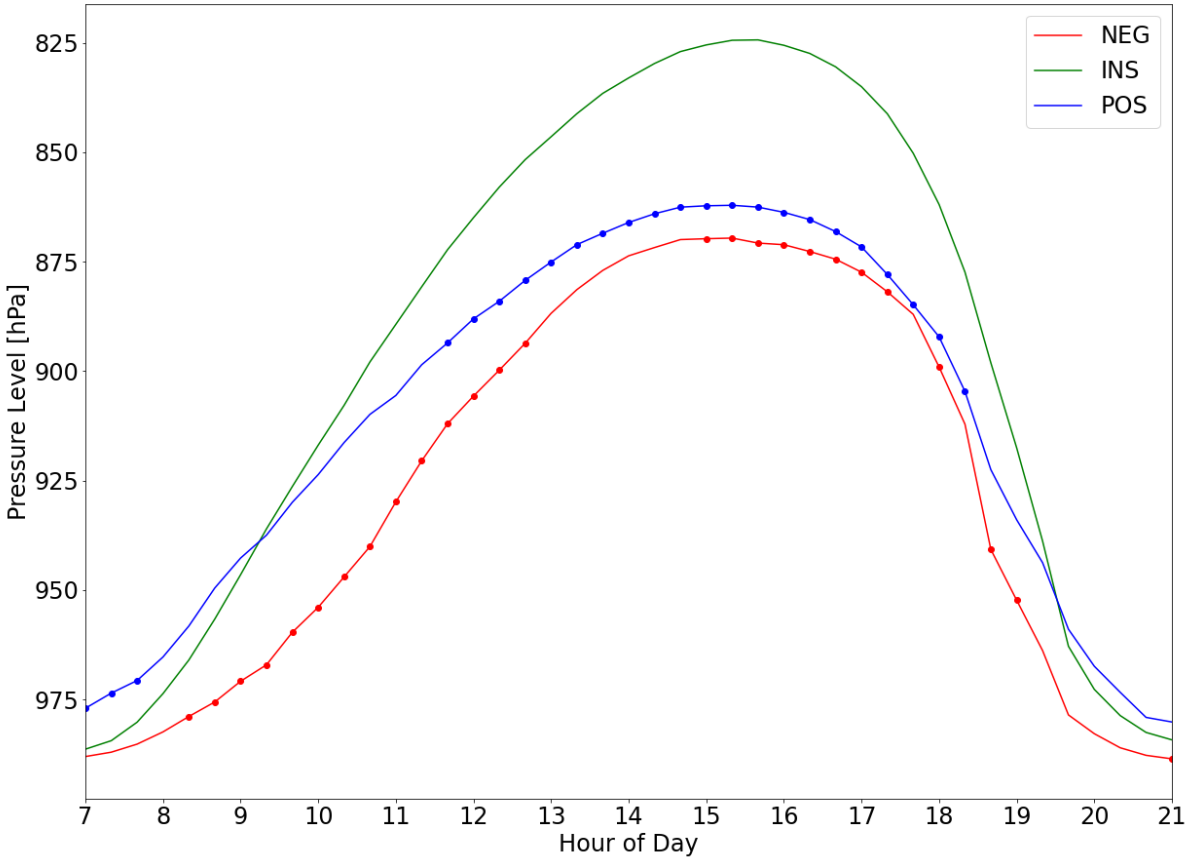

Fig. 4. Mean diurnal cycles of PBL height from near sunrise to near sunset. Timesteps statistically significant from the insensitive regime are marked with points overlaid on the time series.

Accepted for publication in *Journal of Hydrometeorology*. DOI 10.1175/JHM-D-22-0237.1.

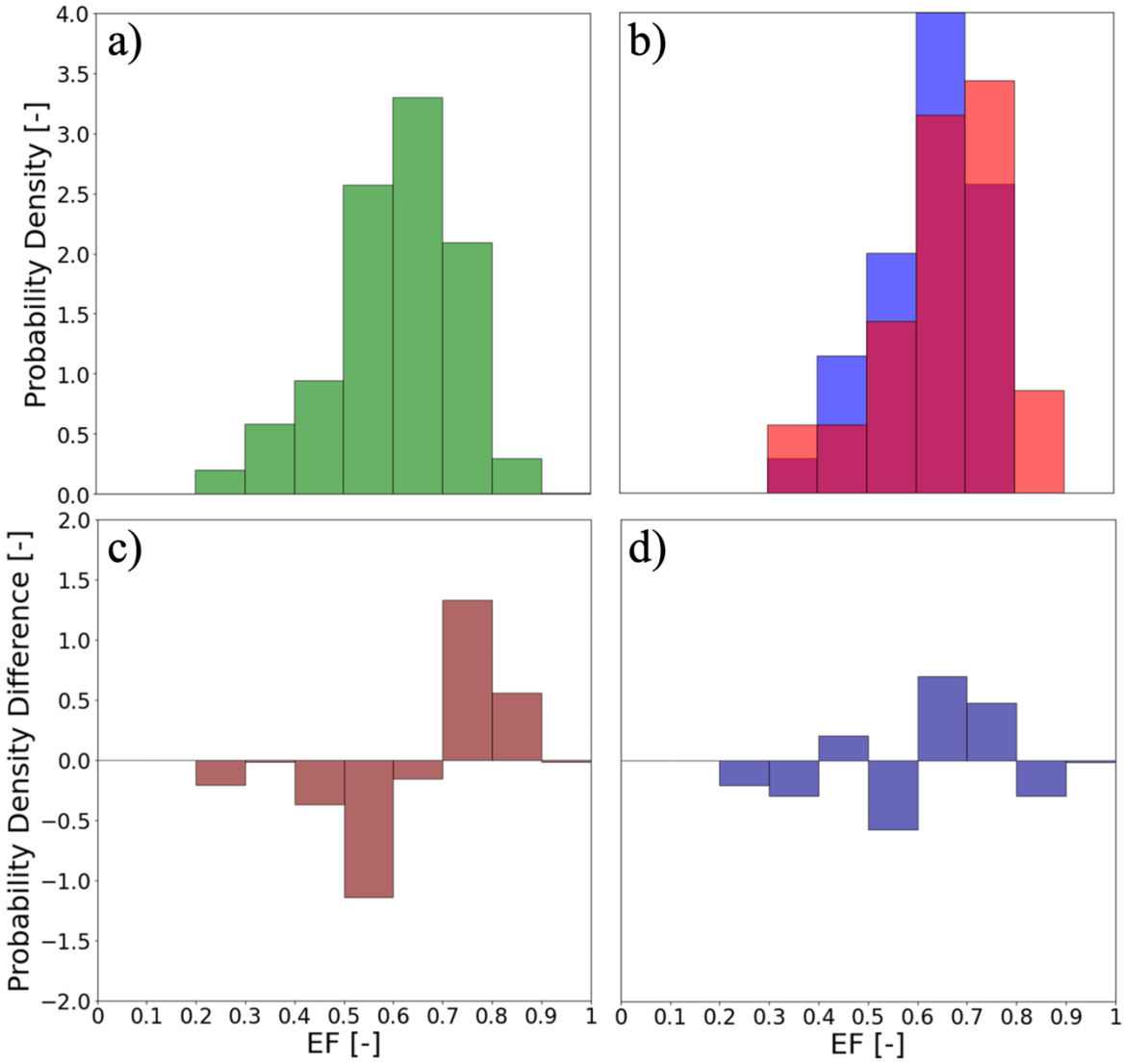

Fig. 5. PDFs of EF from all days in the analysis period (a), only the sensitive days in (b): negative [positive] feedback in red [blue]; differences between negative feedback and insensitive days in (c), between positive feedback and insensitive days in (d).

We next investigate the effects of surface flux partitioning and PBL growth on coupling sensitivity. To do this, we examine composite diurnal cycles of the PBL height (Fig. 4) as well as the distribution of flux partitioning states for insensitive, positive, and negative regimes (Fig. 5).

Negative feedbacks indicate an energy-limited regime (i.e., not moisture limited; evaporation is plentiful), and a shallower PBL reflects this (Seo & Dirmeyer, 2022). Conversely, the positive feedback days tend not to be energy-limited, and they have a more vigorous PBL (Fig. 4), however, they are still both lower than the insensitive days. The differences are significant for both regimes for most of the day, except for the mid-afternoon

Accepted for publication in *Journal of Hydrometeorology*. DOI 10.1175/JHM-D-22-0237.1.

(1300-1500) for the negative regime. This must be due to a higher mid-afternoon variability of the negative regime PBL, since the positive regime is significant during these times, but is closer in magnitude to the insensitive days. Fingerprints of these regimes are also found when considering only the surface contributions to PBL evolution. The top row in Fig. 5 shows distributions of surface evaporative fractions for the entire sample, sensitive positive and negative feedback days shown together, and the bottom row their differences with the insensitive regime. The negative feedback distribution shifts towards larger values of EF (wetter, cooler surfaces; Fig. 5c). This provides further evidence that negative feedback days are more energy-limited. These differences are further elucidated when comparing the two sensitive distributions. Moving from the wet advantage to the dry advantage regime coincides with a shift towards larger EFs (Fig. 5b).

(ii) Mixing Diagrams

We next analyze PBL processes and their role in driving coupling sensitivity. A useful tool for quantifying different source terms (surface fluxes, advection, entrainment, etc.) to PBL evolution is the mixing diagram (Betts, 1992; Santanello et al., 2009). With the assumption of a well-mixed PBL, mixing diagrams can be used to diagnose local land-atmosphere coupling (LoCo) on sub-diurnal time scales (Findell et al., 2017; Seo & Dirmeyer, 2022). They relate near-surface temperature and humidity measurements to the PBL energy balance. This analysis represents a diagnostic that is more sophisticated than parcel theory, but simpler than the prognostic simulation with a single-column model.

We use the lowest model level values of T and Q over the period 0600-1800 LST. The variables are transformed into energy space with the following products: $c_p T$ and λQ, where c_p is the specific heat of dry air (at constant pressure) and λ is the latent heat of vaporization. Plotting hourly timeseries of $c_p T$ against λQ approximates the evolution of these PBL state throughout the day.

To isolate the contributions to the evolution of $c_p T$ and λQ by surface sensible and latent heat fluxes, a vector $\boldsymbol{V}_{sfc}$ is computed. $\boldsymbol{V}_{sfc}$ is defined as:

$$\boldsymbol{V}_{sfc} = \frac{\left\langle \overline{SH}_{sfc}, \overline{LH}_{sfc} \right\rangle}{\varrho_m PBLH} \Delta t \tag{5}$$

Accepted for publication in *Journal of Hydrometeorology*. DOI 10.1175/JHM-D-22-0237.1.

where ρ_m is the mean density within the PBL, PBLH is the PBL height, and Δt is the timestep (Santanello et al., 2009). Additionally, a vector representing the contributions from the mean horizontal advection, $\boldsymbol{V}_{adv}$, may be computed directly from the VARANAL large-scale forcing data. First, we find PBL mean advective tendencies of T and Q by integrating from the surface to the PBL top (using the trapezoidal method) and dividing by the PBL height. These mean tendencies are converted to mean sensible or latent energy inputs [J kg^{-1}] by multiplying by c_p or L, respectively, and Δt. Finally, a residual vector representing the effects of entrainment, radiation, and to a lesser extent the model's relaxation scheme (and other effects) is given by:

$$\boldsymbol{V}_{RER} = \left\langle c_p T \, , \lambda Q \right\rangle_f - \left(\boldsymbol{V}_{sfc} + \boldsymbol{V}_{adv} \right) \tag{6}$$

where RER ≡ Radiation–Entrainment–Relaxation and $\langle c_p T, \lambda Q \rangle_f$ is the state of the PBL at the final timestep (1800 LST). Taking these mean vectors into account, one can quantify the contributions of each component (SFC, ADV, RER) to the heat and moisture content of the PBL. Means over the two subsets of days representing the positive and negative feedback days are taken, as well as their compliment, the subset of "insensitive" days. The composite mixing diagrams are shown in Fig. 6; the mixing diagram for the clear sky days (removed from analysis) are also shown for reference.

Accepted for publication in *Journal of Hydrometeorology*. DOI 10.1175/JHM-D-22-0237.1.

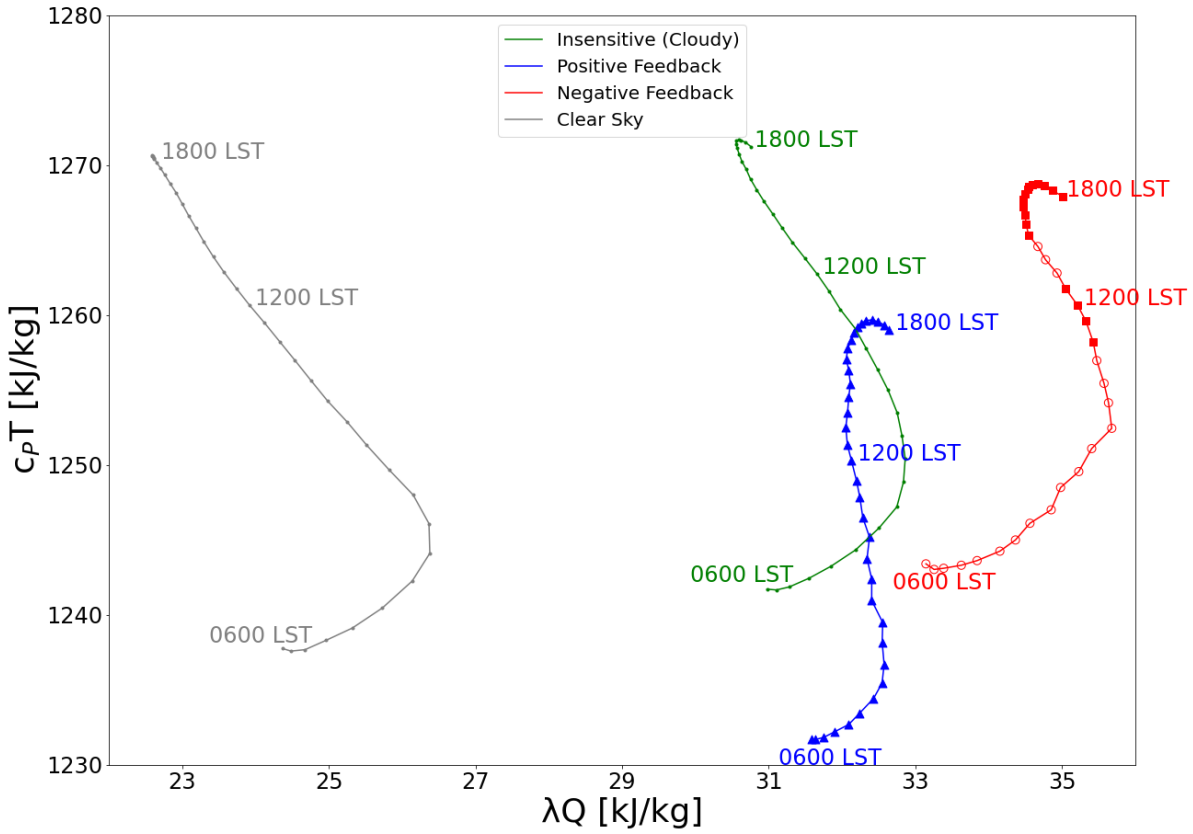

Fig. 6. Composite mixing diagrams for clear sky (grey), insensitive (green), positive feedback (blue), and negative feedback (red) days from 600-1800 LST, each point represents one model timestep (Δt = 20 min.). For positive and negative feedback days, open circles indicate that no statistically significant difference (95% confidence) from the insensitive days is found at this time, squares indicate that only the moisture component (λQ) is significant, and triangles indicate that only the temperature component (c_pT) is significant.

Positive feedback days are significantly cooler than days in the insensitive regime for every timestep. This is mostly due to the cooler initial state of the PBL at 0600 LST, which persists throughout the whole period (Fig. 6). The evolution of the mixing diagram also differs from the insensitive regime. Positive feedback days begin to dry in the morning an hour earlier, at 0820 instead of 0920 LST. Since daytime surface latent heat fluxes moisten the PBL, this earlier drying must be induced by advection, entrainment, or both. However, even though drying begins earlier for the positive regime, it is much weaker than for the insensitive days and changes sign in the afternoon, where a moistening of the PBL is observed after ~1520 LST. This eventually results in a net moistening of 1054 J kg^{-1} for the positive regime, compared to a net drying of -219 J kg-1 for the insensitive regime. The

Accepted for publication in *Journal of Hydrometeorology*. DOI 10.1175/JHM-D-22-0237.1.

positive feedback regime also experiences 2231 J kg^{-1} less heating during the day than the insensitive days.

On negative feedback days, there is initially more moisture content (610 J kg^{-1}) in the PBL, and the initial heat content is comparable to the insensitive days (Fig. 6). In the early morning, this moisture difference is not statistically significant. However, it becomes so at ~1120 LST and remains significant for the rest of the period, with the exception of a one hour period from 1240-1340 LST. This is because of a delayed drying of the PBL, starting at 1000 LST. Drying within the PBL from 1000-1500 LST also occurs at a slower rate when compared to the insensitive days. This is the time when the solar radiation is highest and the PBL is most turbulent, suggesting that advection and/or entrainment of air into the PBL is weaker, the entrained/advected air is less dry, the surface latent heat flux is larger, or a combination of these mechanisms is present. This causes negative feedback days to end the day much wetter than they began, with a total moistening of 1862 J kg^{-1} from 0600-1800 LST; 76% more than the positive feedback days. Negative feedback days also have less heating than positive feedback days (2.45×10^4 vs. 2.73×10^4 J kg^{-1}), suggesting a more energy-limited state.

To further distill the information contained in the composite mixing diagrams, we examine the mean component vectors: $\boldsymbol{V}_{sfc}$, $\boldsymbol{V}_{adv}$, and $\boldsymbol{V}_{RER}$. In Fig. 7, points representing vectors for each positive feedback and negative feedback day overlay two-dimensional histograms representing the probability distribution of the insensitive day vectors. All vectors originate from (0,0). These vectors measure the aggregate contribution to the PBL evolution from each source over the entire time period. Significance for all mixing diagram vectors is tested separately for each dimension (c_pT & λQ).

For positive feedback days, only $\boldsymbol{V}_{adv}$ is statistically significantly different from the insensitive days. Because the surface component is not significant here, the positive feedback days tend to take place nearer to the overall mean state (as opposed to the negative feedback days). Positive feedback days have a mean EF of 0.6272 compared to 0.6273 for the insensitive days (Fig. 7a). For the intermediate part of the range ($0.5 < EF < 0.7$) there are 31 sensitive days, 19 of which are identified as only positive feedback, 9 are only negative feedback, and 3 are both. This suggests that positive feedback days are not usually moisture limited, so what is leading to an increased sensitivity? This brings us to the advective component, $\boldsymbol{V}_{adv}$ (Fig. 7b). Advection provides a noteworthy, aggregate cooling

Accepted for publication in *Journal of Hydrometeorology*. DOI 10.1175/JHM-D-22-0237.1.

effect of -3692 J/kg compared to the insensitive days (- 1147 J/kg). This is 51% of the net cooling difference calculated from the composite mixing diagrams (-2231 J/kg), suggesting that at least half of the additional cooling on positive feedback days is due to advection. More advective cooling like this may make it easier for water vapor to condense into clouds as it rises through the PBL. It should also be noted that there is large spread, however, 27 of the 32 positive feedback days do indeed experience a net cooling through advection. The effect of $\boldsymbol{V}_{RER}$ is not significant for positive feedback days, although again, there is large spread (Fig. 7c).

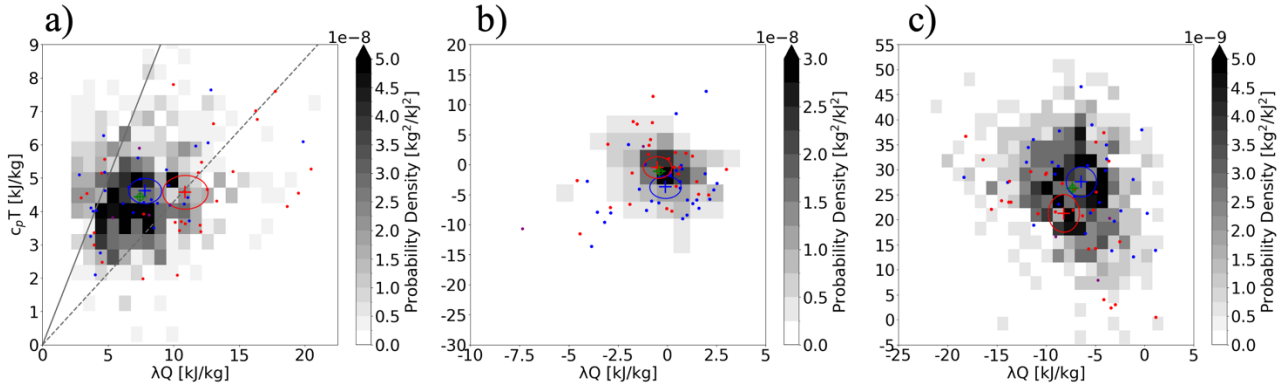

Fig. 7. Termini of daily mixing diagram vectors starting at the origin for: $\mathbf{V}_{\text{sfc}}$ (a), $\mathbf{V}_{\text{adv}}$ (b), and $\mathbf{V}_{\text{RER}}$ (c). Points representing days identified as only positive feedback (blue), only negative feedback (red), and both (purple) overlay a probability distribution of the respective vectors for all other days in the analysis period. Composite vectors for positive feedback days, negative feedback days, and all days are shown with red, blue, and green crosshairs, respectively. Each composite vector crosshair is surrounded by an ellipse representing its 95% confidence interval in the 2-D phase-space of moisture (x-axis) and heat (y-axis). In the left panel, the solid grey line denotes constant EF = 0.5, and the dashed grey line denotes constant EF = 0.7.

For negative feedback days, $\boldsymbol{V}_{sfc}$ and $\boldsymbol{V}_{RER}$ are significantly different from the insensitive days, while $\boldsymbol{V}_{adv}$ is not. These days have more latent energy input from the surface, with comparable amounts of heating, corresponding to a mean EF of 0.697 (Fig. 7a). At the wetter end of the spectrum (EF > 0.7) there are 21 sensitive days, 16 of which are negative feedback only and 5 of which are positive feedback only. This indicates that as the surface EF shifts towards more extreme higher values, the more likely a negative feedback will occur. Considering $\boldsymbol{V}_{RER}$, we see that for negative feedback days there is significantly less warming than usual, 2.07×10^4 J kg^{-1} compared to 2.62×10^4 J kg^{-1} for insensitive days

Accepted for publication in *Journal of Hydrometeorology*. DOI 10.1175/JHM-D-22-0237.1.

(Fig. 7c). It is not straightforward to pin down the exact source of this reduced warming effect due to the multiple contributors to the residual vector; possibilities include cooler entrained air, less incoming radiation due to increased cloud cover, the evaporative cooling of falling precipitation within the PBL, and/or the relaxation scheme used in the simulations. Interestingly, all these named effects (besides model relaxation) tend to occur simultaneously during strong, actively precipitating, mesoscale convective systems (Schumacher & Rasmussen, 2020).

2) DIURNAL CYCLE COMPOSITES

Lastly, we expand our viewpoint from within the PBL to include the free atmosphere above the PBL. For this section, we compute mean diurnal cycles from the CTRL run for the state variables, T and Q, their horizontal advective tendencies, the cloud cover fraction (Fig. 8), and precipitation (Fig. 9). We disregard levels below 200 hPa, assuming that troposphere-stratosphere interactions are not relevant to land-atmosphere interactions.

(i) Positive Feedback Days

From the previous section, positive feedback days are cooler than average within the PBL. This result is reinforced when combined with the composite diurnal cycle of the positive feedback regime. A large, cool anomaly is present from the surface up to about 850 hPa for the entire day (Fig. 8c). There is also a moderate but significant cool anomaly from 450-350 hPa beginning around 1200 LST and lasting throughout the afternoon. Anomalous advective cooling is also seen near the surface for the entire day. This cooling is statistically significant in the morning from 0700-1100 LST, and then again, briefly, from 1540-1620 LST (Fig. 8d). These results are consistent with those in the previous section. Additionally, the day begins significantly cooler than average from the surface to 800 hPa, showing that the initial conditions of the atmosphere play a role as well. While the mixing diagram approach shows no clear moisture limitation within the PBL, there is a significant dry anomaly in the free atmosphere from 750-350 hPa for the first half of the day (Fig. 8a). A significant signal of moist advection helps to alleviate this dryness beginning at 1100 LST (Fig. 8b), however, the air directly above the PBL is still drier than average during the entire day. Therefore, more moisture input is likely to make more of an impact, consistent with a positive feedback regime.

Accepted for publication in *Journal of Hydrometeorology*. DOI 10.1175/JHM-D-22-0237.1.

The dynamics of the system are also important. Anomalous rising motion before sunrise shows that it is not only the surface that is triggering convection (and later cloud formation), but that it may also be induced by large-scale divergence above the PBL prior to sunrise (Fig. 8e). Moving further up into the atmosphere, Fig. 8e shows that there is significant, anomalous subsidence above 800 hPa for most of the day, which is strongest in the early morning hours and from 1000-1300 LST. This may act to stifle deeper convection, restricting cloud cover to just above the PBL. Unsurprisingly, in Fig. 8f, cloud cover fraction anomalies show a decrease in mid- to upper-level cloud cover (above 600 hPa) that is sporadically significant until late afternoon, and an increase in low level clouds directly above the PBL (950-750 hPa) for the entire day. Fig. 9 shows diurnal cycles of precipitation rates, and for the positive feedback days, the convective and total precipitation rates are comparable to insensitive days during the daytime, while the stratiform precipitation rate is significantly reduced in the afternoon (1200-1700 LST). Convective and total precipitation measures also have periods with significantly less precipitation during the early morning and night. These reductions in precipitation may aid in the limitation of available moisture, helping to set up a positive feedback regime.

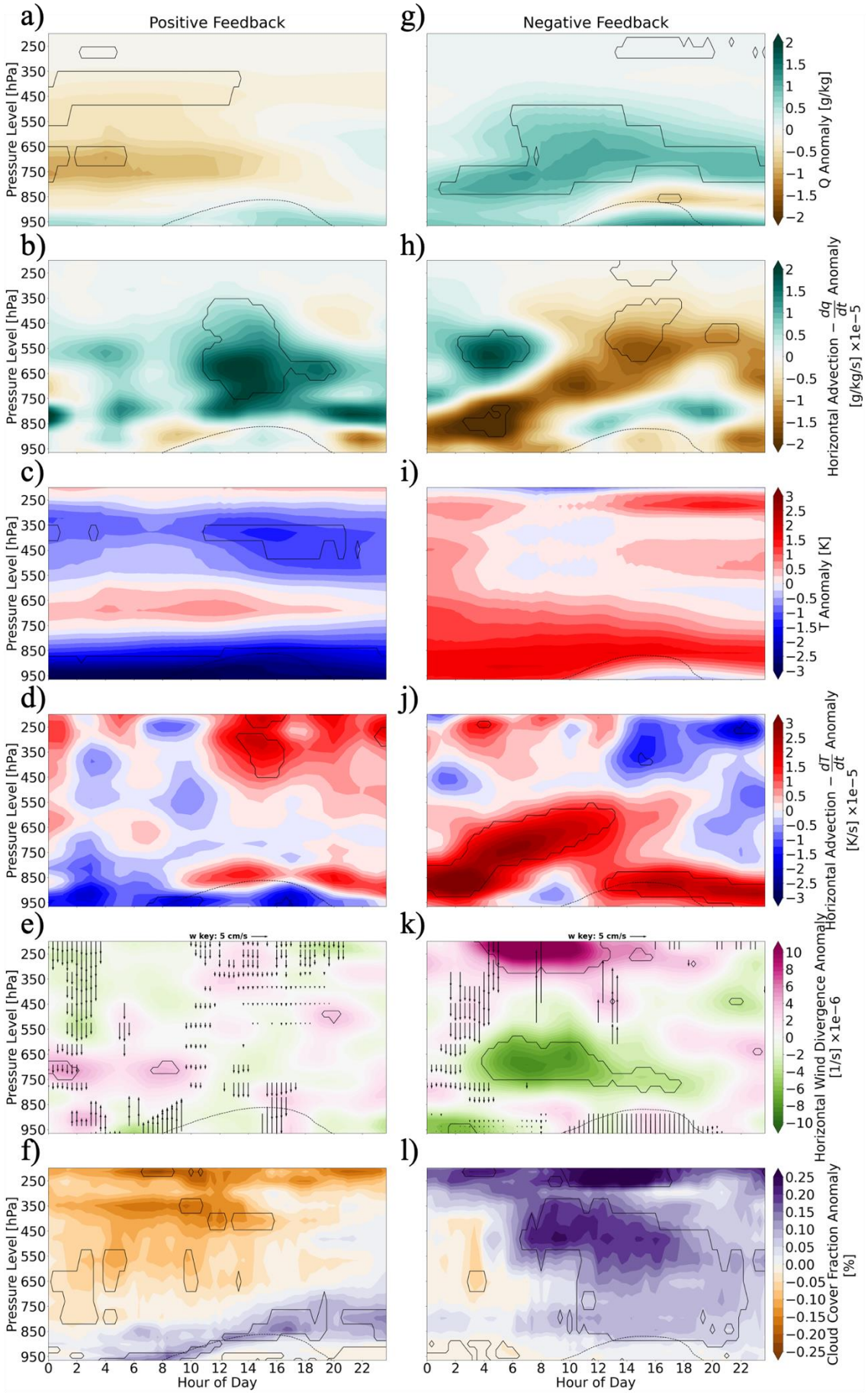

Accepted for publication in *Journal of Hydrometeorology*. DOI 10.1175/JHM-D-22-0237.1.

Fig. 8. Composite diurnal cycles of anomalies for: Q (a,g), T (c,i), the advective tendencies of Q (b,h) and T (d,j), the wind divergence (e,k), and the cloud cover fraction (f,l) for all positive [negative] feedback days in left [right] column. Black contours indicate 95% confidence thresholds. In (e,k), statistically significant (95% confidence) vertical wind anomalies are represented by the black arrows.

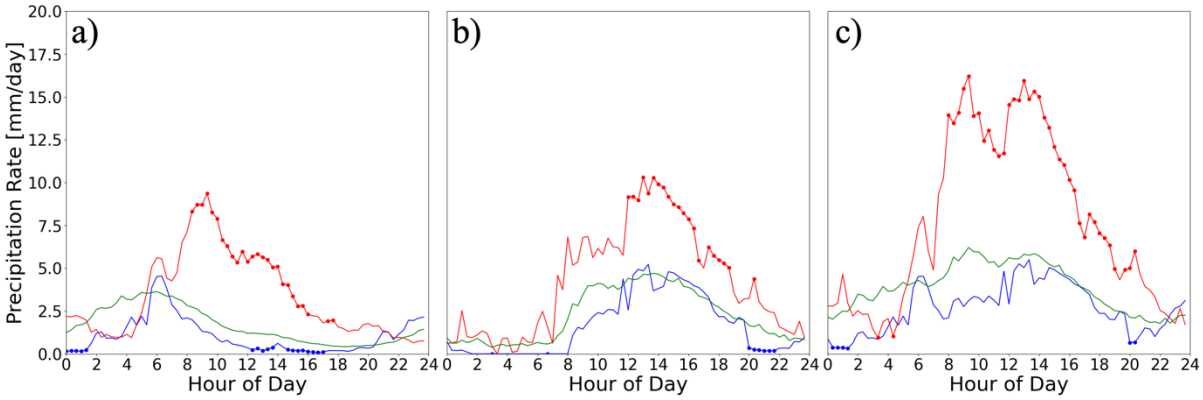

Fig. 9. Composite diurnal cycles of stratiform (a), convective (b), and total (c) precipitation rates. Positive feedback days are shown in blue, negative feedback days in red, and insensitive days in green. Timesteps whose precipitation rate is statistically significant are marked with points overlaid on the time series.

(ii) Negative Feedback Days

The diurnal cycles for the negative feedback regime show stark differences when compared to those of the positive regime. Beginning with Fig. 8g, we see that there is a significant abundance of moisture below 500 hPa all the way to the surface. This, along with a larger amount of moisture input from the surface (as indicated by the mixing diagram), sets up an environment ripe for stronger moist convection and storm activity. Fig. 8i indicates a warmer environment the whole day, although there is no statistical significance. Fig. 8k shows large-scale divergence and vertical velocity anomalies. This result appears to indicate the presence of a large-scale element, such as a squall line, mesoscale convective system (MCS), or other form of deep convection, which begins to pass through the domain before sunrise. This is evidenced by significant convergence (green) at lower levels combined with significant divergence (magenta) at the top of the troposphere beginning at 0600 LST, along with strong vertical velocity anomalies at the mid-levels of the atmosphere near sunrise and during the early afternoon.

Another noteworthy feature is the presence of significant downward velocity anomalies preceding convection. This large-scale subsidence feature has been observed for large,

Accepted for publication in *Journal of Hydrometeorology*. DOI 10.1175/JHM-D-22-0237.1.

precipitating cumulonimbus clouds and may be induced by cloud-scale circulations (Fritsch, 1975; Knupp & Cotton, 1985). This may also be what causes the heating anomaly observed near the surface in Fig. 8j at the same time, as the subsiding air may be heated through adiabatic compression. Another heating anomaly is observed once convection is initiated at mid-levels (800-600 hPa), which may be caused by the latent heat release of condensation within the updraft region (Fig. 8j). Deeper convective activity can also be seen clearly in Fig. 8l, which shows significant anomalies of cloud cover fraction spanning most of the atmosphere above the PBL beginning at 0600 and lasting the rest of the day. Evidence of deeper convection is also seen in Fig. 9, where negative feedback days have significantly more precipitation, both stratiform and convective. The stratiform anomaly, which peaks at 0900 LST, occurs before the convective anomaly, which peaks at 1300 LST. This may indicate the larger system breaching the domain before the actual convective cell passes through. Another important feature in these composites is that most of the features associated with deep convective appear to decay starting in the mid-afternoon around 1400 LST (Fig. 8g, k, & l), making surface heating even more important to maintain convection. In this study, the negative feedback regime is defined so that a lower (higher) EF leads to increased (decreased) convection and cloud formation. Therefore, a shift to a lower (higher) EF leading to increased (decreased) surface heating may act to further energize (decay) these larger systems as they pass over, leading to increased/prolonged (decreased/shortened) convective activity and rainfall. This also provides more evidence for the significance of the RER vector in the mixing diagram method, where effects other than advection most likely play a larger role *within the PBL*, such as increased evaporative cooling, or decreased incoming net radiation (due to increased cloud cover).

4. Discussion and Conclusions

The goal of this study is to develop a method to understand how and under what conditions there is a higher degree of coupling sensitivity between a sub-grid surface states (that may be present in a heterogeneous domain the size of a GCM grid-cell), and the overlying atmosphere. We use SCAM6, a single-column model, to create an ensemble of concurrent simulations over the ARM-SGP site in Northern Oklahoma, using an observationally-based large-scale forcing dataset, VARANAL, to drive the model. All ensemble members have the same atmospheric forcings (i.e., lateral boundary conditions), but separate lower boundary conditions covering a range of prescribed evaporative fractions.

Accepted for publication in *Journal of Hydrometeorology*. DOI 10.1175/JHM-D-22-0237.1.

These boundary conditions are meant to represent the full range of flux partitioning states that may be present in a heterogeneous domain, and therefore overlooked by today's climate models. By evaluating the perturbed surface ensemble members against each other and a control simulation (forced with the observed surface state), we quantify L-A coupling sensitivity.

To our knowledge, this study is unique in analyzing L-A coupling *sensitivity*, rather than just coupling strength and variability, on such short timescales (sub-daily) for a large sample of days over the course of many years. There are many days that show a high degree of sensitivity to variable surface conditions. This strong coupling behavior is expected, because the ARM-SGP site is located within one of the canonical L-A coupling "hotspots" (Koster et al., 2006; Dirmeyer, 2011). Our results also indicate that on these timescales, coupling behavior can shift very quickly. There are multiple days where a positive feedback of EF on the cloud population was dominant, followed by a day with the opposite outcome (a negative feedback). There are also periods of 2-3 days which all had dominant feedbacks of the same sign. This is in line with other studies that have found coupling behavior to have a large range of possible states day-to-day (Roundy et al., 2013; Roundy & Santanello, 2017; Zeng et al., 2019; Yang et al., 2022). In this analysis, positive feedback days have stronger coupling sensitivities on average, indicating that the wet advantage regime is more active/dominant in CESM2, at least for this location. A stronger positive feedback of surface properties such as soil moisture or EF on clouds and precipitation has been found in many other studies when applied to GCMs or coarse regional models (Hohenegger et al., 2009; Taylor et al., 2013; Moon et al., 2019) – although these studies lack the finer temporal resolution used here, often computing L-A coupling metrics by using daily mean values over the entire diurnal cycle.

Even though the positive feedback regime is slightly stronger, days with strong negative feedbacks still occur. By compositing the most sensitive days in each regime, we show that the atmosphere exhibits preferential states and/or boundary conditions that lead to a favored positive or negative feedback. Positive feedback days tend to manifest on days of shallower convection, where such convection's vertical extent is restricted by a strengthened inversion and subsidence above the PBL. The conditions needed to initiate and maintain convection are provided by the large-scale forcing. Therefore, an increase in EF at the surface injects more moisture into the PBL, driving increased cloud content by moistening surface parcels

Accepted for publication in *Journal of Hydrometeorology*. DOI 10.1175/JHM-D-22-0237.1.

that will be lifted by shallow convection. These conditions may be analogous to shallow cumulus or stratocumulus cloud regimes. Negative feedback days tend to manifest on days with existing deep convective systems, possibly caused by mesoscale convective systems or storm fronts passing through the domain. Instead of initiating and increasing cloud production through an increase in PBL moisture content, as in the positive feedback days, the increase in LWP is driven by an enhancement or prolongation of the deeper convective systems through increased sensible heat flux. This process is similar to those identified in observations (Taylor, 2015; Klein & Taylor, 2020; Gaal & Kinter, 2021).

Sensitive feedback days are found around a range of EF close to analyzed values (Zhu et al., 2019) for this location, and behavior such as this has been observed in field campaigns in similar climates (e.g., Lyons et al., 1993). Surface heat fluxes and EF can be highly heterogeneous within domains of a similar size to GCM grid cells (Elhag et al., 2011; Eswar et al., 2013; Chaney et al., 2016; Zhu et al., 2020; Chaney et al., 2021), with length scales of heterogeneity comparable to those known to be most ideal in the initiation of mesoscale circulations (van Heerwaarden et al., 2014). GCMs currently cannot represent such processes, but this study shows that differences in EF can initiate significant shifts in coupling behavior. This kind of L-A coupling is neglected, and accounting for it would likely lead to increased model fidelity. We argue that improved parameterizations that account for these processes that display high sensitivity of coupling behavior to the surface should be a high priority for model development.

It should be noted that the conclusions presented here come with a few caveats. Firstly, these results are only for one location. Similarly, only one model has been used. However, as stated previously, similar results have been found over other locations around the world, using both observations and models other than CESM2. Second, the return leg of the feedback regimes is neglected in this study. In other words, once clouds and precipitation have formed, the feedback of those features on the surface states is lost. Some examples of these feedbacks are radiative cooling underneath the cloud base and the evaporative cooling and the moistening of the surface by precipitation. While these feedbacks may change the results, we are not able to detect them given the prescribed surface conditions. Third, these specific results depend on the quality of the model. The fidelity of the model is an important factor in the conclusions, and its ability to reproduce observations is essential to give

Accepted for publication in *Journal of Hydrometeorology*. DOI 10.1175/JHM-D-22-0237.1.

credence to these results. Finally, the SCAM6 model does not account for the effects of sub-grid scale secondary circulations that may arise from a spatially heterogeneous surface.

Our results describe how the atmospheric column exhibits a sensitivity to a variable surface state, separating it from the secondary effects of induced circulations. Further studies will need to quantify the additional effect of such circulations, once they are initiated by surface heterogeneity. It is our intention to compare these intermediate results to a convective resolving model, such as an LES, to determine if the presence of secondary circulations weaken, enhance, or alter the feedback regimes described in this study. Thus, the mixing diagram analyses, SCM and LES simulations form a continuum of increasing sophistication, which may aid the parameterization improvements we call for above. A more thorough comparison to observations would be ideal. However, field campaigns with sufficient spatial resolution over a long enough period to inform such analysis are lacking. Future observational campaigns aimed at studying land-atmosphere interactions should take this into account, if possible, although we acknowledge that this is a challenging task.

Acknowledgments.

This research was supported by National Oceanic and Atmospheric Administration grants NA19OAR4310242 and NA22OAR4310643 as part of the Coupling Land and Atmospheric Subgrid Parameterizations (CLASP) project within the Global Energy and Water Exchanges (GEWEX) program, a core project of the World Climate Research Programme (WCRP).

Data Availability Statement.

VARANAL large-scale forcing data (Tang et al. 2019) was downloaded from the Atmospheric Radiation Measurement (ARM) Data Discovery tool at https://adc.arm.gov/discovery/#/.

REFERENCES

Avissar, R., and R. A. Pielke, 1989: A Parameterization of Heterogeneous Land Surfaces for Atmospheric Numerical Models and Its Impact on Regional Meteorology. *Monthly*

Weather Review, **117**, 2113–2136, https://doi.org/10.1175/1520-0493(1989)117<2113:APOHLS>2.0.CO;2.

Avissar, R., and T. Schmidt, 1998: An Evaluation of the Scale at which Ground-Surface Heat Flux Patchiness Affects the Convective Boundary Layer Using Large-Eddy Simulations. *Journal of the Atmospheric Sciences*, **55**, 2666–2689, https://doi.org/10.1175/1520-0469(1998)055<2666:AEOTSA>2.0.CO;2.

Benson, D. O., and P. A. Dirmeyer, 2021: Characterizing the Relationship between Temperature and Soil Moisture Extremes and Their Role in the Exacerbation of Heat Waves over the Contiguous United States. *Journal of Climate*, **34**, 2175–2187, https://doi.org/10.1175/JCLI-D-20-0440.1.

Berg, A., K. Findell, B. R. Lintner, P. Gentine, and C. Kerr, 2013: Precipitation Sensitivity to Surface Heat Fluxes over North America in Reanalysis and Model Data. *Journal of Hydrometeorology*, **14**, 722–743, https://doi.org/10.1175/JHM-D-12-0111.1.

Betts, A. K., 1992: FIFE atmospheric boundary layer budget methods. *Journal of Geophysical Research: Atmospheres*, **97**, 18523–18531, https://doi.org/10.1029/91JD03172.

Betts, A. K., 2009: Land-Surface-Atmosphere Coupling in Observations and Models. *Journal of Advances in Modeling Earth Systems*, **1**, 4, https://doi.org/10.3894/JAMES.2009.1.4.

Bezerra, B. G., C. A. C. dos Santos, B. B. da Silva, A. M. Perez-Marin, M. V. C. Bezerra, J. R. C. Bezerra, and T. V. R. Rao, 2013: Estimation of soil moisture in the root-zone from remote sensing data. *Rev. Bras. Ciênc. Solo*, **37**, 596–603, https://doi.org/10.1590/S0100-06832013000300005.

Bosman, P. J. M., C. C. van Heerwaarden, and A. J. Teuling, 2019: Sensible heating as a potential mechanism for enhanced cloud formation over temperate forest. *Quarterly Journal of the Royal Meteorological Society*, **145**, 450–468, https://doi.org/10.1002/qj.3441.

Brunsell, N. A., 2006: Characterization of land-surface precipitation feedback regimes with remote sensing. *Remote Sensing of Environment*, **100**, 200–211, https://doi.org/10.1016/j.rse.2005.10.025.

Budyko, M. I., 1974: *Climate and life*. New York: Academic Press, xvii, 508 p. pp.

Accepted for publication in *Journal of Hydrometeorology*. DOI 10.1175/JHM-D-22-0237.1.

Catalano, F., A. Alessandri, M. De Felice, Z. Zhu, and R. B. Myneni, 2016: Observationally based analysis of land–atmosphere coupling. *Earth Syst. Dynam.*, **7**, 251–266, https://doi.org/10.5194/esd-7-251-2016.

Chaney, N. W., P. Metcalfe, and E. F. Wood, 2016: HydroBlocks: a field-scale resolving land surface model for application over continental extents. *Hydrological Processes*, **30**, 3543–3559, https://doi.org/10.1002/hyp.10891.

——, L. Torres-Rojas, N. Vergopolan, and C. K. Fisher, 2021: HydroBlocks v0.2: enabling a field-scale two-way coupling between the land surface and river networks in Earth system models. *Geoscientific Model Development*, **14**, 6813–6832, https://doi.org/10.5194/gmd-14-6813-2021.

Chen, J., S. Hagos, H. Xiao, J. D. Fast, and Z. Feng, 2020: Characterization of Surface Heterogeneity-Induced Convection Using Cluster Analysis. *Journal of Geophysical Research: Atmospheres*, **125**, e2020JD032550, https://doi.org/10.1029/2020JD032550.

Dal Gesso, S., and R. a. J. Neggers, 2018: Can We Use Single-Column Models for Understanding the Boundary Layer Cloud-Climate Feedback? *Journal of Advances in Modeling Earth Systems*, **10**, 245–261, https://doi.org/10.1002/2017MS001113.

Dirmeyer, P. A., 2011: The terrestrial segment of soil moisture–climate coupling. *Geophysical Research Letters*, **38**, L16702, https://doi.org/10.1029/2011GL048268.

——, and H. E. Norton, 2018: Indications of Surface and Sub-Surface Hydrologic Properties from SMAP Soil Moisture Retrievals. *Hydrology*, **5**, 36, https://doi.org/10.3390/hydrology5030036.

——, F. J. Zeng, A. Ducharne, J. C. Morrill, and R. D. Koster, 2000: The Sensitivity of Surface Fluxes to Soil Water Content in Three Land Surface Schemes. *Journal of Hydrometeorology*, **1**, 121–134, https://doi.org/10.1175/1525-7541(2000)001<0121:TSOSFT>2.0.CO;2.

——, G. Balsamo, E. M. Blyth, R. Morrison, and H. M. Cooper, 2021: Land-Atmosphere Interactions Exacerbated the Drought and Heatwave Over Northern Europe During Summer 2018. *AGU Advances*, **2**, e2020AV000283, https://doi.org/10.1029/2020AV000283.

Accepted for publication in *Journal of Hydrometeorology*. DOI 10.1175/JHM-D-22-0237.1.

Efron, B., 1987: Better Bootstrap Confidence Intervals. *Journal of the American Statistical Association*, **82**, 171–185, https://doi.org/10.2307/2289144.

——, and R. J. Tibshirani, 1994: *An Introduction to the Bootstrap*. Chapman and Hall/CRC, 456 pp, https://doi.org/10.1201/9780429246593.

Ek, M., and L. Mahrt, 1994: Daytime Evolution of Relative Humidity at the Boundary Layer Top. *Monthly Weather Review*, **122**, 2709–2721, https://doi.org/10.1175/1520-0493(1994)122<2709:DEORHA>2.0.CO;2.

Ek, M. B., and A. a. M. Holtslag, 2004: Influence of Soil Moisture on Boundary Layer Cloud Development. *Journal of Hydrometeorology*, **5**, 86–99, https://doi.org/10.1175/1525-7541(2004)005<0086:IOSMOB>2.0.CO;2.

Elhag, M., A. Psilovikos, I. Manakos, and K. Perakis, 2011: Application of the Sebs Water Balance Model in Estimating Daily Evapotranspiration and Evaporative Fraction from Remote Sensing Data Over the Nile Delta. *Water Resour Manage*, **25**, 2731–2742, https://doi.org/10.1007/s11269-011-9835-9.

Entekhabi, D., 1995: Recent advances in land-atmosphere interaction research. *Reviews of Geophysics*, **33**, 995–1003, https://doi.org/10.1029/95RG01163.

Eswar, R., M. Sekhar, and B. K. Bhattacharya, 2013: A simple model for spatial disaggregation of evaporative fraction: Comparative study with thermal sharpened land surface temperature data over India. *Journal of Geophysical Research: Atmospheres*, **118**, 12029-12044, https://doi.org/10.1002/2013JD020813.

Findell, K. L., and E. A. B. Eltahir, 2003a: Atmospheric Controls on Soil Moisture–Boundary Layer Interactions. Part I: Framework Development. *Journal of Hydrometeorology*, **4**, 552–569, https://doi.org/10.1175/1525-7541(2003)004<0552:ACOSML>2.0.CO;2.

——, and ——, 2003b: Atmospheric Controls on Soil Moisture–Boundary Layer Interactions. Part II: Feedbacks within the Continental United States. *J. Hydrometeor.*, **4**, 570–583, https://doi.org/10.1175/1525-7541(2003)004<0570:ACOSML>2.0.CO;2.

——, P. Gentine, B. R. Lintner, and C. Kerr, 2011: Probability of afternoon precipitation in eastern United States and Mexico enhanced by high evaporation. *Nature Geoscience*, **4**, 434–439, https://doi.org/10.1038/ngeo1174.

Accepted for publication in *Journal of Hydrometeorology*. DOI 10.1175/JHM-D-22-0237.1.

——, A. Berg, P. Gentine, J. P. Krasting, B. R. Lintner, S. Malyshev, J. A. Santanello, and E. Shevliakova, 2017: The impact of anthropogenic land use and land cover change on regional climate extremes. *Nat Commun*, **8**, 989, https://doi.org/10.1038/s41467-017-01038-w.

Ford, T. W., C. O. Wulff, and S. M. Quiring, 2014: Assessment of observed and model-derived soil moisture-evaporative fraction relationships over the United States Southern Great Plains. *Journal of Geophysical Research: Atmospheres*, **119**, 6279–6291, https://doi.org/10.1002/2014JD021490.

——, P. A. Dirmeyer, and D. O. Benson, 2018: Evaluation of heat wave forecasts seamlessly across subseasonal timescales. *npj Clim Atmos Sci*, **1**, 1–9, https://doi.org/10.1038/s41612-018-0027-7.

Fritsch, J. M., 1975: Cumulus dynamics: Local compensating subsidence and its implications for cumulus parameterization. *PAGEOPH*, **113**, 851–867, https://doi.org/10.1007/BF01592963.

Gaal, R., and J. L. Kinter III, 2021: Soil Moisture Influence on the Incidence of Summer Mesoscale Convective Systems in the U.S. Great Plains. *Monthly Weather Review*, **149**, 3981–3994, https://doi.org/10.1175/MWR-D-21-0140.1.

Gettelman, A., J. E. Truesdale, J. T. Bacmeister, P. M. Caldwell, R. B. Neale, P. A. Bogenschutz, and I. R. Simpson, 2019: The Single Column Atmosphere Model Version 6 (SCAM6): Not a Scam but a Tool for Model Evaluation and Development. *Journal of Advances in Modeling Earth Systems*, **11**, 1381–1401, https://doi.org/10.1029/2018MS001578.

Guo, Z., and P. A. Dirmeyer, 2013: Interannual Variability of Land–Atmosphere Coupling Strength. *Journal of Hydrometeorology*, **14**, 1636–1646, https://doi.org/10.1175/JHM-D-12-0171.1.

Harvey, N. J., C. L. Daleu, R. A. Stratton, R. S. Plant, S. J. Woolnough, and A. J. Stirling, The impact of surface heterogeneity on the diurnal cycle of deep convection. *Quarterly Journal of the Royal Meteorological Society*, **148**, 3509-3527, https://doi.org/10.1002/qj.4371.

Heerwaarden, C. C. van, J. Vilà-Guerau de Arellano, A. F. Moene, and A. A. M. Holtslag, 2009: Interactions between dry-air entrainment, surface evaporation and convective

Accepted for publication in *Journal of Hydrometeorology*. DOI 10.1175/JHM-D-22-0237.1.

boundary-layer development. *Quarterly Journal of the Royal Meteorological Society*, **135**, 1277–1291, https://doi.org/10.1002/qj.431.

Heerwaarden, C. C. van, J. V.-G. de Arellano, A. Gounou, F. Guichard, and F. Couvreux, 2010: Understanding the Daily Cycle of Evapotranspiration: A Method to Quantify the Influence of Forcings and Feedbacks. *Journal of Hydrometeorology*, **11**, 1405–1422, https://doi.org/10.1175/2010JHM1272.1.

Heerwaarden, C. C. van, J. P. Mellado, and A. D. Lozar, 2014: Scaling Laws for the Heterogeneously Heated Free Convective Boundary Layer. *Journal of the Atmospheric Sciences*, **71**, 3975–4000, https://doi.org/10.1175/JAS-D-13-0383.1.

Hohenegger, C., P. Brockhaus, C. S. Bretherton, and C. Schär, 2009: The Soil Moisture–Precipitation Feedback in Simulations with Explicit and Parameterized Convection. *Journal of Climate*, **22**, 5003–5020, https://doi.org/10.1175/2009JCLI2604.1.

Hsu, H., and P. A. Dirmeyer, 2022: Deconstructing the Soil Moisture–Latent Heat Flux Relationship: The Range of Coupling Regimes Experienced and the Presence of Nonlinearity within the Sensitive Regime. *Journal of Hydrometeorology*, **23**, 1041–1057, https://doi.org/10.1175/JHM-D-21-0224.1.

Huang, H.-Y., and S. A. Margulis, 2009: On the impact of surface heterogeneity on a realistic convective boundary layer. *Water Resources Research*, **45**, 1-16, https://doi.org/10.1029/2008WR007175.

——, and ——, 2013: Impact of soil moisture heterogeneity length scale and gradients on daytime coupled land-cloudy boundary layer interactions. *Hydrological Processes*, **27**, 1988–2003, https://doi.org/10.1002/hyp.9351.

Huang, L., J. H. Jiang, Z. Wang, H. Su, M. Deng, and S. Massie, 2015: Climatology of cloud water content associated with different cloud types observed by A-Train satellites. *Journal of Geophysical Research: Atmospheres*, **120**, 4196–4212, https://doi.org/10.1002/2014JD022779.

Huang, M., P.-L. Ma, N. W. Chaney, D. Hao, G. Bisht, M. D. Fowler, V. E. Larson, and L. R. Leung, 2022: Representing surface heterogeneity in land–atmosphere coupling in E3SMv1 single-column model over ARM SGP during summertime. *Geoscientific Model Development*, **15**, 6371–6384, https://doi.org/10.5194/gmd-15-6371-2022.

Accepted for publication in *Journal of Hydrometeorology*. DOI 10.1175/JHM-D-22-0237.1.

Kang, S.-L., and G. H. Bryan, 2011: A Large-Eddy Simulation Study of Moist Convection Initiation over Heterogeneous Surface Fluxes. *Monthly Weather Review*, **139**, 2901–2917, https://doi.org/10.1175/MWR-D-10-05037.1.

——, and J.-H. Ryu, 2016: Response of moist convection to multi-scale surface flux heterogeneity. *Quarterly Journal of the Royal Meteorological Society*, **142**, 2180–2193, https://doi.org/10.1002/qj.2811.

Kawashima, S., and T. Ishida, 1992: Effects of regional temperature, wind speed and soil wetness on spatial structure of surface air temperature. *Theor Appl Climatol*, **46**, 153–161, https://doi.org/10.1007/BF00866095.

Kim, M.-S., and B. H. Kwon, 2019: Estimation of Sensible Heat Flux and Atmospheric Boundary Layer Height Using an Unmanned Aerial Vehicle. *Atmosphere*, **10**, 363, https://doi.org/10.3390/atmos10070363.

Klein, C., and C. M. Taylor, 2020: Dry soils can intensify mesoscale convective systems. *Proceedings of the National Academy of Sciences*, **117**, 21132–21137, https://doi.org/10.1073/pnas.2007998117.

Knupp, K. R., and W. R. Cotton, 1985: Convective cloud downdraft structure: An interpretive survey. *Reviews of Geophysics*, **23**, 183–215, https://doi.org/10.1029/RG023i002p00183.

Koster, R. D., and M. J. Suarez, 1992: Modeling the land surface boundary in climate models as a composite of independent vegetation stands. *Journal of Geophysical Research: Atmospheres*, **97**, 2697–2715, https://doi.org/10.1029/91JD01696.

——, and Coauthors, 2006: GLACE: The Global Land–Atmosphere Coupling Experiment. Part I: Overview. *Journal of Hydrometeorology*, **7**, 590–610, https://doi.org/10.1175/JHM510.1.

Lawrence, D. M., and Coauthors, 2019: The Community Land Model Version 5: Description of New Features, Benchmarking, and Impact of Forcing Uncertainty. *Journal of Advances in Modeling Earth Systems*, **11**, 4245–4287, https://doi.org/10.1029/2018MS001583.

Accepted for publication in *Journal of Hydrometeorology*. DOI 10.1175/JHM-D-22-0237.1.

Lee, J. M., Y. Zhang, and S. A. Klein, 2019: The Effect of Land Surface Heterogeneity and Background Wind on Shallow Cumulus Clouds and the Transition to Deeper Convection. *J. Atmos. Sci.*, **76**, 401–419, https://doi.org/10.1175/JAS-D-18-0196.1.

Letzel, M. O., and S. Raasch, 2003: Large Eddy Simulation of Thermally Induced Oscillations in the Convective Boundary Layer. *Journal of the Atmospheric Sciences*, **60**, 2328–2341, https://doi.org/10.1175/1520-0469(2003)060<2328:LESOTI>2.0.CO;2.

Lyons, T. J., P. Schwerdtfeger, J. M. Hacker, I. J. Foster, R. C. G. Smith, and H. Xinmei, 1993: Land-Atmosphere Interaction in a Semiarid Region: The Bunny Fence Experiment. *Bulletin of the American Meteorological Society*, **74**, 1327–1334, https://doi.org/10.1175/1520-0477(1993)074<1327:LIIASR>2.0.CO;2.

Ma, H.-Y., Chuang, C., Klein, S., Lo, M.-H., Zhang, Y., Xie, S., Zheng, X., Ma, P.-L., Zhang, Y., and Phillips, T., 2015: An improved hindcast approach for evaluation and diagnosis of physical processes in global climate models, *Journal of Advances in Modeling Earth Systems*, **7**, 1810-1827, https://doi.org/10.1002/2015MS000490.

Machulskaya, E., and D. Mironov, 2018: Boundary Conditions for Scalar (Co)Variances over Heterogeneous Surfaces. *Boundary-Layer Meteorol*, **169**, 139–150, https://doi.org/10.1007/s10546-018-0354-6.

Ma, H.-Y., C. C. Chuang, S. A. Klein, M.-H. Lo, Y. Zhang, S. Xie, X. Zheng, P.-L. Ma, Y. Zhang, and T. J. Phillips, 2015: An improved hindcast approach for evaluation and diagnosis of physical processes in global climate models. *Journal of Advances in Modeling Earth Systems*, **7**, 1810–1827, https://doi.org/10.1002/2015MS000490.

Manabe, S., J. Smagorinsky, and R. F. Strickler, 1965: SIMULATED CLIMATOLOGY OF A GENERAL CIRCULATION MODEL WITH A HYDROLOGIC CYCLE. *Monthly Weather Review*, **93**, 769–798, https://doi.org/10.1175/1520-0493(1965)093<0769:SCOAGC>2.3.CO;2.

Norton, H., 2018: Soil Moisture Memory (SMM) of Karst and Non-karst Soils. George Mason University, 132 pp. https://www.proquest.com/docview/2205469678/abstract/CF2616199EBA466APQ/1 (Accessed November 23, 2022).

Accepted for publication in *Journal of Hydrometeorology*. DOI 10.1175/JHM-D-22-0237.1.

Omidvar, H., E. Bou-Zeid, Q. Li, J.-P. Mellado, and P. Klein, 2020: Plume or bubble? Mixed-convection flow regimes and city-scale circulations. *Journal of Fluid Mechanics*, **897**, A5, https://doi.org/10.1017/jfm.2020.360.

Qian, Y., M. Huang, B. Yang, and L. K. Berg, 2013: A Modeling Study of Irrigation Effects on Surface Fluxes and Land–Air–Cloud Interactions in the Southern Great Plains. *Journal of Hydrometeorology*, **14**, 700–721, https://doi.org/10.1175/JHM-D-12-0134.1.

Qiu, S., and I. N. Williams, 2020: Observational Evidence of State-Dependent Positive and Negative Land Surface Feedback on Afternoon Deep Convection Over the Southern Great Plains. *Geophysical Research Letters*, **47**, e2019GL086622, https://doi.org/10.1029/2019GL086622.

Roundy, J. K., and E. F. Wood, 2015: The Attribution of Land–Atmosphere Interactions on the Seasonal Predictability of Drought. *J. Hydrometeor.*, **16**, 793–810, https://doi.org/10.1175/JHM-D-14-0121.1.

——, and J. A. Santanello, 2017: Utility of Satellite Remote Sensing for Land–Atmosphere Coupling and Drought Metrics. *J. Hydrometeor.*, **18**, 863–877, https://doi.org/10.1175/JHM-D-16-0171.1.

——, C. R. Ferguson, and E. F. Wood, 2013: Temporal Variability of Land–Atmosphere Coupling and Its Implications for Drought over the Southeast United States. *J. Hydrometeor.*, **14**, 622–635, https://doi.org/10.1175/JHM-D-12-090.1.

Roy, S. B., and R. Avissar, 2000: Scales of response of the convective boundary layer to land-surface heterogeneity. *Geophysical Research Letters*, **27**, 533–536, https://doi.org/10.1029/1999GL010971.

Santanello, J. A., C. D. Peters-Lidard, S. V. Kumar, C. Alonge, and W.-K. Tao, 2009: A Modeling and Observational Framework for Diagnosing Local Land–Atmosphere Coupling on Diurnal Time Scales. *J. Hydrometeor.*, **10**, 577–599, https://doi.org/10.1175/2009JHM1066.1.

——, and Coauthors, 2018: Land–Atmosphere Interactions: The LoCo Perspective. *Bulletin of the American Meteorological Society*, **99**, 1253–1272, https://doi.org/10.1175/BAMS-D-17-0001.1.

Accepted for publication in *Journal of Hydrometeorology*. DOI 10.1175/JHM-D-22-0237.1.

Seo, E., and P. A. Dirmeyer, 2022: Understanding the diurnal cycle of land–atmosphere interactions from flux site observations. *Hydrology and Earth System Sciences*, **26**, 5411–5429, https://doi.org/10.5194/hess-26-5411-2022.

Shin, S.-H., and K.-J. Ha, 2007: Effects of Spatial and Temporal Variations in PBL Depth on a GCM. *Journal of Climate*, **20**, 4717–4732, https://doi.org/10.1175/JCLI4274.1.

Shukla, J., and Y. Mintz, 1982: Influence of Land-Surface Evapotranspiration on the Earth's Climate. *Science*, **215**, 1498–1501, https://doi.org/10.1126/science.215.4539.1498.

Simon, J. S., A. D. Bragg, P. A. Dirmeyer, and N. W. Chaney, 2021: Semi-Coupling of a Field-Scale Resolving Land-Surface Model and WRF-LES to Investigate the Influence of Land-Surface Heterogeneity on Cloud Development. *Journal of Advances in Modeling Earth Systems*, **13**, e2021MS002602, https://doi.org/10.1029/2021MS002602.

Sposito, G., 2017: Understanding the Budyko Equation. *Water*, **9**, 236, https://doi.org/10.3390/w9040236.

Tang, S., C. Tao, S. Xie, and M. Zhang, 2019: *Description of the ARM Large-Scale Forcing Data from the Constrained Variational Analysis (VARANAL) Version 2*.

Tawfik, A. B., P. A. Dirmeyer, and J. A. Santanello, 2015a: The Heated Condensation Framework. Part I: Description and Southern Great Plains Case Study. *Journal of Hydrometeorology*, **16**, 1929–1945, https://doi.org/10.1175/JHM-D-14-0117.1.

——, ——, and ——, 2015b: The Heated Condensation Framework. Part II: Climatological Behavior of Convective Initiation and Land–Atmosphere Coupling over the Conterminous United States. *Journal of Hydrometeorology*, **16**, 1946–1961, https://doi.org/10.1175/JHM-D-14-0118.1.

Taylor, C. M., 2015: Detecting soil moisture impacts on convective initiation in Europe. *Geophysical Research Letters*, **42**, 4631–4638, https://doi.org/10.1002/2015GL064030.

——, and R. J. Ellis, 2006: Satellite detection of soil moisture impacts on convection at the mesoscale. *Geophysical Research Letters*, **33**, L03404, https://doi.org/10.1029/2005GL025252.

——, C. E. Birch, D. J. Parker, N. Dixon, F. Guichard, G. Nikulin, and G. M. S. Lister, 2013: Modeling soil moisture-precipitation feedback in the Sahel: Importance of spatial scale

Accepted for publication in *Journal of Hydrometeorology*. DOI 10.1175/JHM-D-22-0237.1.

versus convective parameterization. *Geophysical Research Letters*, **40**, 6213–6218, https://doi.org/10.1002/2013GL058511.

Tian, J., Y. Zhang, S. A. Klein, R. Öktem, and L. Wang, 2022: How Does Land Cover and Its Heterogeneity Length Scales Affect the Formation of Summertime Shallow Cumulus Clouds in Observations From the US Southern Great Plains? *Geophysical Research Letters*, **49**, e2021GL097070, https://doi.org/10.1029/2021GL097070.

Ukkola, A. M., A. J. Pitman, M. G. Donat, M. G. De Kauwe, and O. Angélil, 2018: Evaluating the Contribution of Land-Atmosphere Coupling to Heat Extremes in CMIP5 Models. *Geophysical Research Letters*, **45**, 9003–9012, https://doi.org/10.1029/2018GL079102.

Wei, J., J. Zhao, H. Chen, and X.-Z. Liang, 2021: Coupling Between Land Surface Fluxes and Lifting Condensation Level: Mechanisms and Sensitivity to Model Physics Parameterizations. *Journal of Geophysical Research: Atmospheres*, **126**, e2020JD034313, https://doi.org/10.1029/2020JD034313.

Williams, I. N., and M. S. Torn, 2015: Vegetation controls on surface heat flux partitioning, and land-atmosphere coupling. *Geophysical Research Letters*, **42**, 9416–9424, https://doi.org/10.1002/2015GL066305.

Xie, S., R. T. Cederwall, and M. Zhang, 2004: Developing long-term single-column model/cloud system–resolving model forcing data using numerical weather prediction products constrained by surface and top of the atmosphere observations. *Journal of Geophysical Research: Atmospheres*, **109**, D01104, https://doi.org/10.1029/2003JD004045.

Yang, C., Y. Ma, and Y. Yuan, 2021: Terrestrial and Atmospheric Controls on Surface Energy Partitioning and Evaporative Fraction Regimes Over the Tibetan Plateau in the Growing Season. *Journal of Geophysical Research: Atmospheres*, **126**, e2021JD035011, https://doi.org/10.1029/2021JD035011.

——, ——, ——, and H. Zuo, 2022: Positive and Negative Surface Feedback and Atmospheric Control of Land Surface Conditions on Convective Organization Over the Tibetan Plateau. *Journal of Geophysical Research: Atmospheres*, **127**, e2022JD036884, https://doi.org/10.1029/2022JD036884.

Accepted for publication in *Journal of Hydrometeorology*. DOI 10.1175/JHM-D-22-0237.1.

Zeng, D., X. Yuan, and J. K. Roundy, 2019: Effect of Teleconnected Land–Atmosphere Coupling on Northeast China Persistent Drought in Spring–Summer of 2017. *Journal of Climate*, **32**, 7403–7420, https://doi.org/10.1175/JCLI-D-19-0175.1.

Zhang, S., X. Yang, W. Zhang, S. Li, and Y. Zhang, 2019: Sensitivity of afternoon precipitation to evaporative fraction in eastern Asia based on ERA-Interim datasets. *Atmospheric Science Letters*, **20**, e892, https://doi.org/10.1002/asl.892.

Zheng, Y., H. Zhang, and Z. Li, 2021: Role of Surface Latent Heat Flux in Shallow Cloud Transitions: A Mechanism-Denial LES Study. *Journal of the Atmospheric Sciences*, **78**, 2709–2723, https://doi.org/10.1175/JAS-D-20-0381.1.

Zhu, W., S. Jia, and A. Lv, 2019: A Statistical Analysis of the Remotely Sensed Land Surface Temperature–Vegetation Index Method for the Retrieval of Evaporative Fraction Over Grasslands in the Southern Great Plains. *IEEE Journal of Selected Topics in Applied Earth Observations and Remote Sensing*, **12**, 2889–2896, https://doi.org/10.1109/JSTARS.2019.2917183.

——, ——, U. Lall, Y. Cheng, and P. Gentine, 2020: An observation-driven optimization method for continuous estimation of evaporative fraction over large heterogeneous areas. *Remote Sensing of Environment*, **247**, 111887, https://doi.org/10.1016/j.rse.2020.111887.

Accepted for publication in *Journal of Hydrometeorology*. DOI 10.1175/JHM-D-22-0237.1.